This dissertation has been
microfilmed exactly as received 67-1782

MUEHLLEHNER, Gerd, 1939-

THE ^{208}PB(D,T)^{207}PB REACTION WITH 15 TO 25 MEV DEUTERONS.

The University of Michigan, Ph.D., 1966
Physics, nuclear

University Microfilms, Inc., Ann Arbor, Michigan

THE ^{208}PB(D,T) ^{207}PB REACTION WITH 15 TO 25 MEV DEUTERONS

by
Gerd Muehllehner

A dissertation submitted in partial fulfillment
of the requirements for the degree of
Doctor of Philosophy in the
University of Michigan
1966

Doctoral Committee:

Professor W.C. Parkinson, Chairman
Assistant Professor H.J. Fischbeck
Professor K.T. Hecht
Professor J.S. King
Associate Professor R.S. Tickle

THE ^{208}PB(D,T)^{207}PB REACTION WITH 15 TO 25 MEV DEUTERONS

By Gerd Muehllehner

The purpose of the work described in the dissertation was to determine experimentally the absolute differential cross-sections for the (d,t) reaction on ^{208}Pb corresponding to transitions to single particle levels in ^{207}Pb for incident deuterons in the energy range from 15 to 25 MeV and to determine the set of parameters in the Distorted Wave Born Approximation (DWBA) calculations that give the best fit to the measured differential cross-sections. The reaction ^{208}Pb(d,t)^{207}Pb is well suited for this purpose in as much as ^{208}Pb has a closed shell in both protons and neutrons and therefore the low lying levels excited in the (d,t) reaction should correspond to pure single particle hole states. Given the set of parameters the method can then be used to extract spectroscopic information from measured differential cross-sections for reactions in other nuclei in this mass region where other than single particle transitions are involved.

Deuterons from The University of Michigan 83-inch cyclotron were used to measure absolute differential cross-sections at 14.8 MeV, 20.1 MeV and 24.8 MeV for six single particle levels in ^{207}Pb and for elastic scattering of deuterons on ^{208}Pb. The level at an excitation energy of 3.42 MeV was identified as the $h_{9/2}$ single particle state. The reaction products were analyzed in energy with a magnetic spectrometer and recorded either with a sonic spark chamber or in nuclear emulsion or with a plastic scintillator and photomultiplier. The DWBA calculations were performed at the Oak Ridge National Laboratory with the aid of Dr. R. H. Bassel using the computer code called Julie.

The DWBA calculations were performed for several values of the bound neutron parameters $\underline{a}$, R_o and λ, several values of the triton distorted wave parameters W_o and R_o' and different forms of the interaction.

It was found that the measured distributions could be matched well with the calculated distributions in shape as well as absolute cross-section. The only major discrepancy was found for the $i_{13/2}$ at the lower energies and at forward angles.

Changing the triton parameters W_o and R_o' affects the shape of the distributions at the forward angles, particularly for the $i_{13/2}$. It was necessary to vary W_o with energy in order to obtain equally good fits to the absolute cross-section at all three energies. The neutron parameters $\underline{a}$ and R_o were found to affect the absolute cross-section

only. Calculations which included corrections for finite range and non-local effects did not improve the fit to the absolute cross-section.

Using the best set of parameters as determined in this investigation it was found that the shape of the calculated angular distributions agrees well with the measured distributions. The absolute differential cross-sections differ by as much as 28 %. It is concluded therefore that the DWBA analysis will be useful in extracting ℓ-values and spectroscopic factors in the heavy mass region for deuterons of energy 15 to 25 MeV.

ACKNOWLEDGMENTS

The author wishes to express his gratitude to the chairman of his doctoral committee, Professor W. C. Parkinson, for his guidance and constructive criticism which was essential to the success of this work. Thanks are also due to the remaining members of the doctoral committee for their aid during various stages of the work. He is grateful to Mr. A. Poltorak for the many helpful discussions concerning all aspects.

The author is indebted to Dr. R. H. Bassel for his valuable assistance in the computations and for the many discussions of the results, as well as for making the computer program "Julie" of the Oak Ridge National Laboratory available.

The fine cooperation of Mr. W. E. Downer and the rest of the cyclotron staff has been very helpful; the plate reading of Mrs. Goldie Sanders is particularly appreciated.

The research described in this dissertation has been supported in part by the U.S. Atomic Energy Commission.

TABLE OF CONTENTS

		PAGE
ACKNOWLEDGMENTS		ii
LIST OF TABLES		v
LIST OF ILLUSTRATIONS		vi
CHAPTER		
I	INTRODUCTION	1
II	EXPERIMENT	4
	1. THE CYCLOTRON	4
	2. TARGETS	4
	3. PARTICLE DETECTION SYSTEMS	7
	4. PROCEDURE	14
	5. DIFFERENTIAL CROSS-SECTION	18
III	THEORY	21
	1. SHELL MODEL	21
	2. ^{208}PB(D,T)^{207}PB AND THE SHELL MODEL	23
	3. TRANSITION AMPLITUDE	23
	4. DISTORTED WAVES	28
	5. NUCLEAR MATRIX ELEMENT	31
	6. CROSS-SECTION	37
	7. INVERSE REACTION	38
IV	RESULTS AND DISCUSSION	40
	1. SPECTRUM	40
	2. ANGULAR DISTRIBUTIONS	42
	3. DWBA CALCULATIONS	54

PAGE

CHAPTER

V SUMMARY AND CONCLUSION 63

REFERENCES 65

LIST OF TABLES

TABLE		PAGE
I.	Isotopic Composition of Target Material	6
II.	Excitation Energies and Q-Value	43
III.	Deuteron Energies	44
IV.	DWBA Parameters Used to Obtain Best Fit to Measured Distributions	44
V.	Spectroscopic Factors	52
VI.	Variation of Differential Cross-Section with Neutron Parameters R_o and $\underline{a}$	58
VII.	Variation of Differential Cross-Section with Triton Parameters W_o and R_o'	58
VIII.	Variation of Differential Cross-Section with Finite Range and Non-Local Corrections	60

LIST OF ILLUSTRATIONS

FIGURE		PAGE
1.	Cyclotron Floor Plan	5
2.	Energy Loss of 5.48 MeV α-particles in Lead Foils	19
3.	Block Diagram of Spark Chamber Electronics	10
4.	Proportional Counter Spectra	12
5.	Total and Relative Solid Angle of Reaction Products Magnet	16
6.	Target Angle for Maximum Resolution for (d,t) Reaction on Lead	19
7.	Level Diagram	24
8.	Typical Spectra Obtained in the Reaction $^{208}Pb(d,t)^{207}Pb$ at a Deuteron Energy of 24.8 MeV	41
9.	Angular Distribution for 14.8 MeV Deuterons Elastically Scattered from ^{208}Pb	45
10.	Angular Distribution for 20.1 MeV Deuterons Elastically Scattered from ^{208}Pb	46
11.	Angular Distribution for 24.8 MeV Deuterons Elastically Scattered from ^{208}Pb	47
12.	Angular Distribution of Triton Groups in the Reaction $^{208}Pb(d,t)^{207}Pb$ at a Deuteron Energy of 14.8 MeV	49
13.	Angular Distribution of Triton Groups in the Reaction $^{208}Pb(d,t)^{207}Pb$ at a Deuteron Energy of 20.1 MeV	50
14.	Angular Distribution of Triton Groups in the Reaction $^{208}Pb(d,t)^{207}Pb$ at a Deuteron Energy of 24.8 MeV	51
15.	Angular Distribution of $h_{9/2}$ at 20.1 MeV	53
16.	Effect of Triton Parameters W_o and R_o' on Shape of Distribution of $i_{13/2}$	57
17.	Energy Dependence of $f_{5/2}$ at 15 MeV	61
18.	Energy Dependence of $f_{5/2}$ at 25.1 MeV	62

CHAPTER I
INTRODUCTION

In the study of the structure of the nucleus, nuclear reactions have been and continue to be an important source of information. In attempting to account for the observable properties of nuclei models such as the Shell model have been constructed; nuclear reactions are then described in terms of these models. Such a description has been particularly successful for direct reactions, in which an incoming particle interacts with the target nucleus and another particle is emitted without the formation of an intermediate or compound nucleus. In this case the reaction proceeds with a minimum rearrangement taking place within the target nucleus.

To date the most successful description of direct reactions is given by the Distorted Wave Born Approximation (DWBA) analysis, which permits the calculation of the differential cross-section for a transition from the ground state of the target nucleus to a state in the final nucleus. In the DWBA analysis the transition amplitude is calculated; the relative motion of the interacting particles is described by distorted waves before and after the collision and the potential responsible for the interaction is simplified in order to facilitate the calculations. The DWBA analysis has proven to be useful in extracting from experimental data spectroscopic information such as the orbital angular momentum and transition probabilities, in the region where it has been tested. The method has not been tested however, because of a lack of data, in the region of the higher mass nuclei and at energies above the Coulomb barrier.

The purpose of the work described in this dissertation was to determine experimentally the absolute differential cross-sections for the (d,t) reaction on ^{208}Pb corresponding to transitions to single particle levels in ^{207}Pb for incident deuterons in the energy range from 15 to 25 MeV and to determine the set of parameters in the DWBA calculations that give the best fit to the measured differential cross-sections. The reaction ^{208}Pb(d,t)^{207}Pb is well suited for this purpose, as ^{208}Pb has a closed shell in both protons and neutrons and therefore the low lying levels excited in the (d,t) reaction should correspond to pure single particle hole states. Given the set of parameters the method can then be used to extract spectroscopic information from measured differential cross-sections for reactions in other nuclei in this mass region where other than single particle transitions are involved.

Deuterons from The University of Michigan 83-inch cyclotron were used to measure absolute differential cross-sections at 14.8 MeV, 20.1 MeV, and 24.8 MeV for six single particle levels in ^{207}Pb and for elastic scattering of deuterons on ^{208}Pb. The reaction products were analysed in energy with a magnetic spectrometer and recorded either with a sonic spark chamber or in nuclear emulsions or with a plastic scintillator and photomultiplier. The DWBA calculations were performed at the Oak Ridge National Laboratory with the aid of Dr. R. H. Bassel using the computer program called Julie.

It was found that in general the shapes of the calculated and measured angular distributions were in good agreement for a wide range of parameters forall levels except the $i_{13/2}$. For this level the shape was not matched well at the forward angles at 14.8 MeV; it was however,

in better agreement at 20.1 MeV, and improved still further at 24.8 MeV. The best set of parameters gave rather good agreement with the measured absolute differential cross-sections, the largest difference being 28 %.

CHAPTER II

EXPERIMENT

1. THE CYCLOTRON

The general features of the 83-inch cyclotron of The University of Michigan have been described previously [1]; only a short summary is given here. The cyclotron is a variable energy sector-focused machine designed to produce beams of protons, deuterons and alpha particles of maximum energies of 35 MeV, 40 MeV and 80 MeV respectively. The beam extracted from the cyclotron is passed through a beam preparation system consisting of two 110° double focusing magnets, which have a combined dispersion of 5 kev/mm at 40 MeV. The energy spread of the beam in the scattering chamber is determined by slits located midway between the two focusing magnets and in the scattering chamber. The reaction products analysis system consists of three magnets, each of wedge angle 180°, $n = -(R/B)\,(dB/dR) = \frac{1}{2}$ and a radius of curvature of 133 cm. The first of the three magnets covers a momentum range of 6 % with one current setting and with a 1 mm slit in the scattering chamber provides an ion-optical resolution of $E/\Delta E = 2.67 \times 10^{3}$. The analysis system can be rotated about an axis through the center of the scattering chamber to any angle from -10° to $+ 125^{\circ}$ and further with slight modifications. A floor plan of the facilities is shown in Figure 1.

2. TARGETS

All of the targets used in these measurements were prepared using

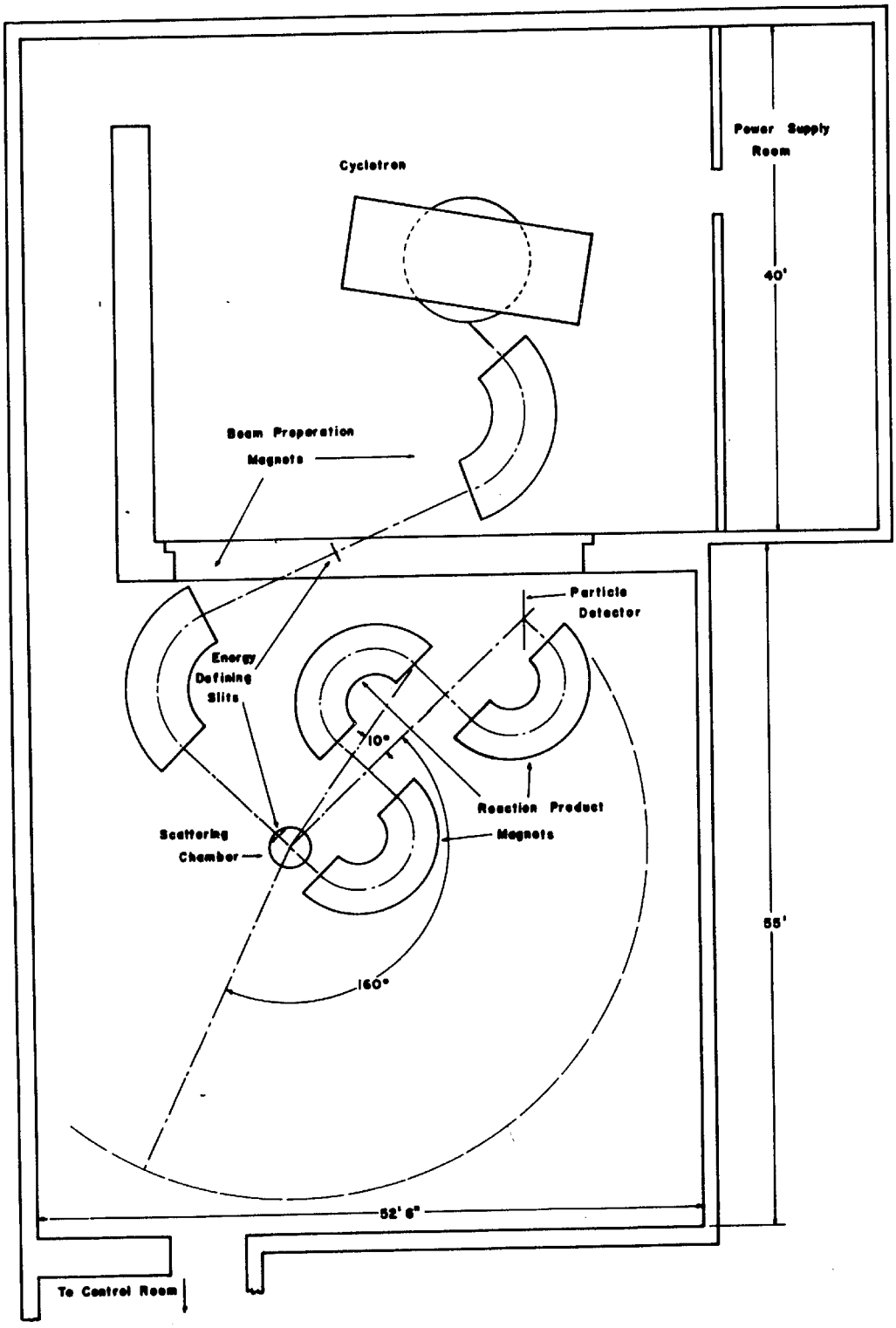

FIGURE 1 - Cyclotron Floor Plan

lead in metal form enriched in mass 208 and obtained from the Oak Ridge National Laboratory. The isotopic composition is listed in Table I.

TABLE I

Isotopic Composition of Target Material

Isotope	Atomic Percent	Precision
204	< 0.05	--
206	0.19	± 0.05
207	0.52	± 0.05
208	99.3	± 0.05

The lead was evaporated using an electron gun evaporator onto a glass slide thinly coated with a weak soap solution. The glass slide was attached to a water-cooled cooper plate approximately three inches above the crucible. The lead film was then floated off the glass slide by slowly submerging the slide into water and letting the soap dissolve. The film was then picked up on a cooper frame.

The thickness of the targets was determined by measuring the energy loss of α-particles passing through the targets. An ^{241}Am source which emits α-particles of 5.48 MeV was mounted in a small vacuum chamber below a rotating target holder on which the lead targets were placed. The energy of the α-particles was determined with a silicon surface barrier detector and pulse height analyzer.

To determine experimentally the relation between the thickness of lead films and the energy loss of the α-particles, the thickness of several natural lead films was determined by weighing small portions of known area on a microbalance. The measured energy loss was then plotted as a function of target thickness. The graph shown in Figure 4 is in good agreement with the results of theoretical calculations [3].

3. PARTICLE DETECTION SYSTEMS

Three types of detectors were used to locate and count the particles arriving at the focal surface of the reaction products magnet. These are A) nuclear emulsions, B) a plastic scintillator with a photomultiplier tube, C) a sonic spark chamber. Each will be discussed in terms of their relative advantages and disadvantages.

A. Nuclear Emulsions: The emulsions used in these experiments were Ilford type K-2 nuclear track plates. These consists of an emulsion 100 microns thick on a glass substrate one inch wide by ten inches long. Three such plates are placed end to end to cover the full width of the focal surface illuminated by the reaction products magnet. Because the focal surface of the first magnet is tilted at an angle of 49.7^{o} with respect to the normal to the optic axis, the particles pass through approximately 155 microns of emulsion. To give continuous and dense tracks the tritons were slowed down by aluminium absorbers to approximately 12 MeV before entering the emulsion, deuterons were slowed down to about 7 MeV. The nuclear emulsion has the advantage that

every particle entering it is recorded; it provides a permanent record with essentially no error in the recording of the particles. Many problems, however, arise in trying to obtain an accurate count of the number of tracks per unit length along the plate. This is normally done by counting individual tracks as seen under a microscope. Due to the fact that the focal surface is tilted with respect to the optic axis between 25 and 30 percent of all tracks are only partially visible in the field of view of the microscope. In order to obtain an accurate count, partial and complete tracks were counted separately. Another difficulty arises from the fact that the human error in counting increases at high track densities. The most severe limitation of nuclear emulsions, however, is the length of time necessary to extract the information.

B. Plastic Scintillator: This particle detector consists of a plastic scintillator mounted on a photomultiplier tube. A particle entering and stopping in the scintillator produces a light flash, which is converted into a voltage pulse in the photomultiplier tube. The amplitude of the pulse is proportional to the energy deposited in the scintillator by the particle. The output pulses from the photomultiplier are amplified and analysed in height with a multi-channel analyser. Such detectors have the advantage that dead times are short and counting losses are of consequence only at very high counting rates. The principal disadvantage is the low energy resolution. When used with the magnetic spectrometer only one particle group can be counted at a time. For this reason the method was used only in measuring angular distributions of elastically scattered deuterons.

C. Sonic Spark Chamber: The spark chamber, 30 inches long and six inches high, is identical in mechanical design to the one developed at the University of Rochester [2]. It consists of two sections, a proportional counter and a spark gap. A particle arriving at the focal surface of the spectrometer magnet first passes through the proportional counter and then into the spark gap. The proportional counter serves two functions; first, it is used to identify the kind of particle to be detected while discriminating against all others, and second, the pulse from the counter is used to apply the high potential across the spark gap. At the time the high potential is applied a time-to-pulse-height converter is turned on. The particle having passed through the proportional counter enters the sparkgap where it leaves an ionization trail. As a result, when the high potential is applied, a spark discharge occurs in the region of the trail. The sonic waves associated with the spark travel down the spark gap to a transducer mounted at one end. The signal from the transducer, after appropriate shaping, is used to turn off the time-to-pulse-height converter. The output pulses of the converter, the height of which is proportional to the distance from the transducer to the point at which the particle crossed the gap, are analyzed in height in a multi-channel analyzer. Figure 2 shows a block diagram of the device with the associated electronics.

The proportional counter is 25 inches long and has a two mil thick aluminium entrance window, a three mil diamter tungsten wire and a one mil thick aluminium exit window. The spark gap is three mm in depth. The transducer is acoustically isolated with respect to the walls. Both, the proportional counter and the spark gap are filled with a gas

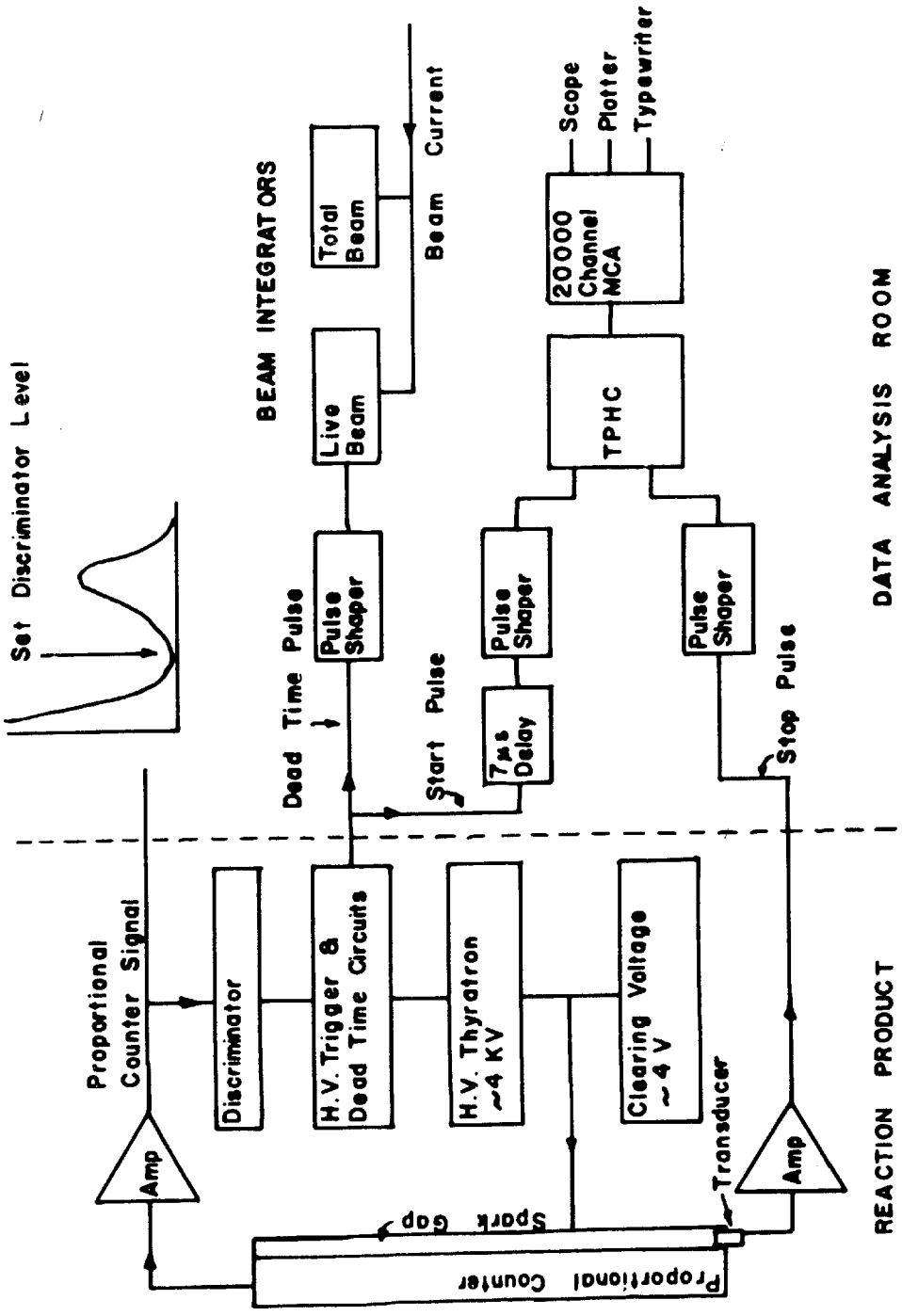

FIGURE 3 - Block Diagram of Spark Chamber Electronics

mixture of 10 % argon and 90 % neon at a pressure of approximately five pounds above atmospheric. The gas supply bottle is connected to the chamber permanently to maintain constant pressure. Small leaks in the chamber result in a slow steady flow of gas from the bottle through the chamber, preventing a buildup of impurities.

The central wire of the proportional counter, operated at a positive potential of 800 to 1000 volts, is coupled through a capacitance to a preamplifier and amplifier which has a lower level discriminator. The particles were slowed with the aid of aluminium absorbers in order to improve the signal-to-noise ratio. This has the added advantage that particles with the same magnetic rigidity but of different mass and/or charge either do not penetrate the absorber or produce pulses of lower amplitude and do not pass the discriminator. Typical spectra from the proportional counter for different particles all of energy 20.1 MeV are shown as a function of absorber in Figure 3. From the proportional counter spectrum the discriminator level is determined so as to ensure that every pulse caused by the type of particle to be counted passes the discriminator.

The discriminator output pulse is fed into a trigger circuit which fires a thyratron tube and applies the high voltage (approximately four kV) to the spark gap. After the high voltage is applied a gating circuit inhibits another pulse from reapplying the high voltage for a period of three milliseconds, which is slightly longer than the maximum time necessary to analyse a particle. Following the spark discharge the residual ions are swept out of the gap by a low (approximately four volts) clearing voltage. The transducer pulse is amplified and used to trigger a multivibrator, which produces a pulse whose shape is accept-

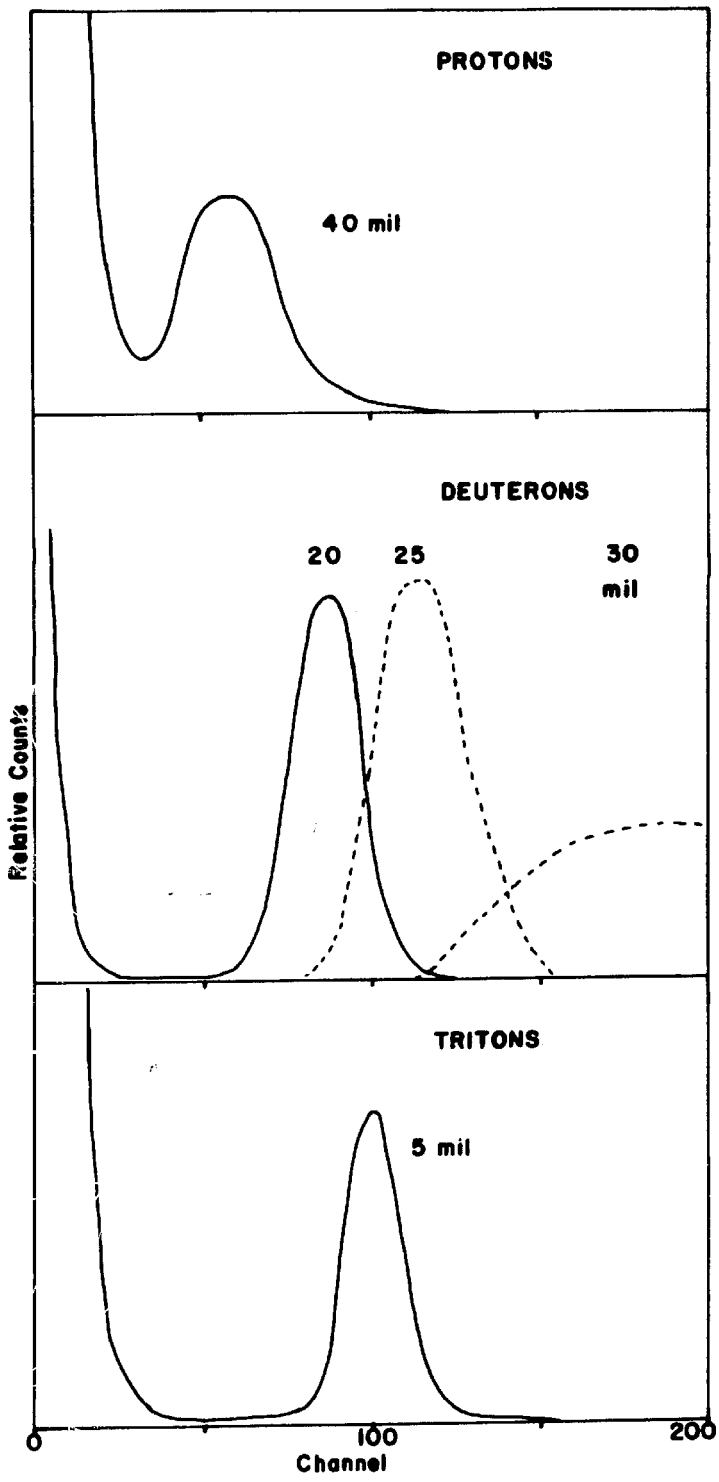

FIGURE 4 - Proportional Counter Spectra

able to the time-to-pulse-height (TPH) converter. The TPH converter is started by the differentiated leading edge of the three millisecond deadtime pulse, which occurs at the time of application of the high voltage. The output pulses of the TPH converter are then analysed according to height in a multi-channel analyzer.

In using the spark chamber great care has to be taken to get an accurate count of the number of particles entering it. If the discriminator of the proportional counter amplifier is set with care then the number of pulses arriving at the trigger circuit will be equal to the number of particles entering the chamber plus the number of background pulses which are high enough to pass the discriminator. The number of applications of the high voltage without a subsequent spark, which corresponds to start pulses without stop pulses, gives an indication of the efficiency if the background pulses are taken into consideration. The correct settings for the high voltage and the clearing voltage, both of which affect the efficiency, are determined by observing their effect on the number of start pulses without corresponding stop pulses. It was found that the maximum efficiency obtainable was very nearly 100 %.

The advantage of such a device over plates or scintillator is obvious. The results are immediately available on an oscilloscope display and can be plotted or typed out in numerical form. The spark chamber, however, has several disadvantages. Counting rates must be kept low to ensure reliable operation. The resolution as used in this application is poor. Because of the three mm depth of the chamber particles entering at a point result in a peak seven mm wide at half height. Further, even with paraffin shielding the background is such that it is not possible to measure levels of less than five μb/str. at 20 MeV.

However, of the three particle detection systems used the spark chamber is the most suitable provided the resolution required is not less than approximately 55 kev.

A typical spectrum taken with the spark chamber is shown in Figure 8 together with the same spectrum taken with a nuclear emulsion. It is evident that the background is higher and the resolution lower for the spark chamber. The counts in the low channels are due to noise originating in the electronics and the counts at the left end of the spectrum are due to start pulses without corresponding stop pulses.

4. PROCEDURE

The differential cross-sections were measured every five degrees from a minimum angle of 10 degrees to a maximum angle of 100 degrees except at 15 MeV where they were taken every five degrees from 10 to 50 degrees and every 10 degrees from 50 to 100 degrees. All angular distributions were taken both with nuclear emulsions and with the spark chamber.

The absolute solid angle of the magnetic spectrometer and the change of solid angle across the focal surface was determined as follows. First, a baffle whose opening was measured accurately was inserted in front of the spectrometer magnet. The opening of the baffle was small enough to ensure that all particles passing through it would reach the detection device and would not be stopped or scattered by the surfaces of the magnet gap. A spectrum was taken under these conditions. The same spectrum was repeated with the baffle removed and with different openings of the permanent horizontal slit located at the entrance of the magnet. Thus the solid angle was determined for different slit openings. To determine the change in solid angle across the focal sur-

face the spectrum was shifted in small steps across the surface. The results are shown in Figure 5a and 5b.

The beam current through the target was measured with a Faraday cup and current integrator. The integrator was calibrated and a least-squares analysis indicated a deviation from linearity of less than 0.6 %, systematic errors are estimated to be less than 1 %. For measurements at angles less than 10^{o} the Faraday cup was removed and a silicon surface barrier detector mounted at -45^{o} to the incoming beam was used. The monitor counter was calibrated against the current integrator at angles above 10^{o} and the two methods were found to agree with each other to better than 2 %. Whenever the spark chamber was used another integrator was employed which included a gating circuit. Current through the target was integrated only during the time the spark chamber was ready to analyse another particle by applying the three millisecond deadtime pulse of the chamber to the gating circuit of the integrator. The two integrators agreed with each other to within 0.3 %.

The energy of the incoming beam was determined in the following way: a small volume at the edge of the magnetic field of the first reaction products magnet was shimmed to obtain an essentially uniform magnetic field. Two nuclear magnetic resonance probes were mounted in this volume. These probes are used to set the magnetic field in the magnet gap and due to the fact that a magnetic resonance device is used the absolute magnetic field can be measured accurately. The ratio of the magnetic field in the shimmed volume to the magnetic field in the center of the gap was measured with the aid of a Hall effect device. From the magnetic field necessary to center elastically scattered deuterons the energy of the incoming deuterons was calculated taking

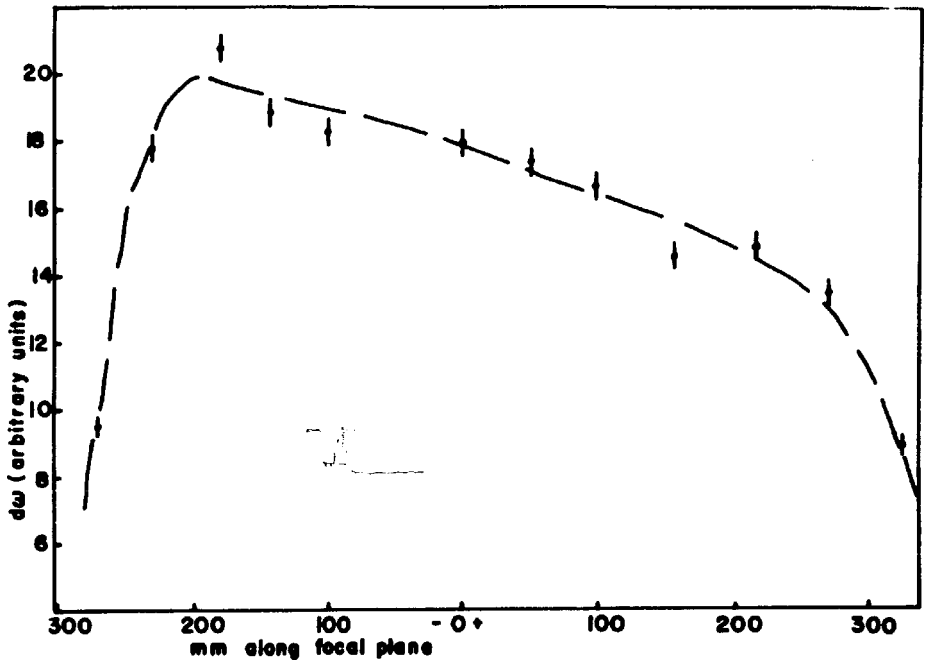

FIGURE 5a - Relative Solid Angle of Reaction Products Magnet (Magnet Aperture = 4°)

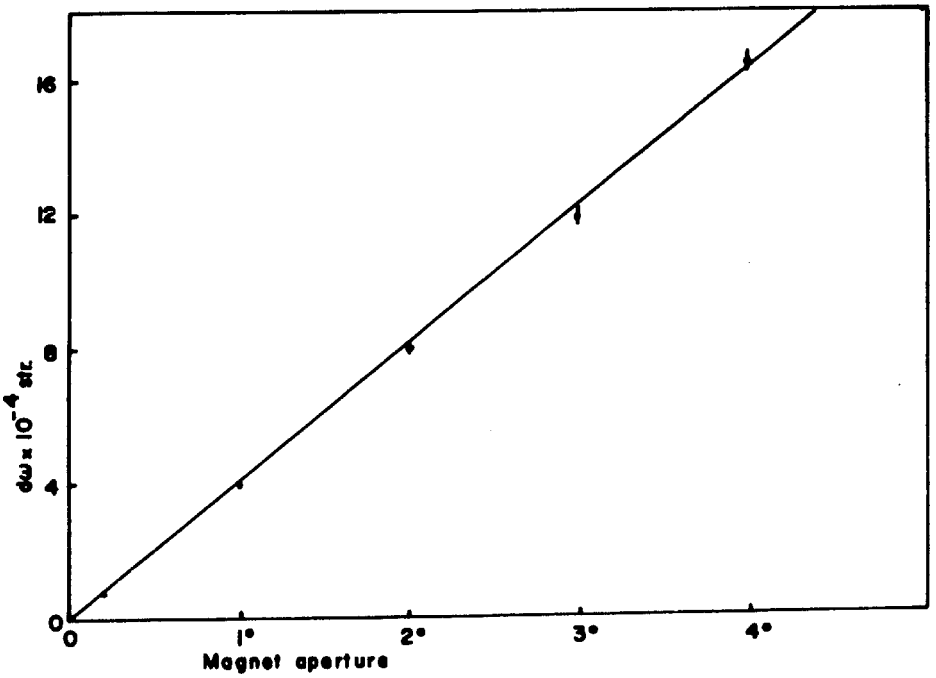

FIGURE 5b - Absolute Solid Angle of Reaction Products Magnet

into account the scattering angle and energy losses in the target. Due to variations of the magnetic field along the path of the particles and because no attempt was made to take into account the fringe field at the entrance and exit of the magnet the method is an approximate one only. The resultant values are estimated to be accurate to $\pm$ 1 % only.

Recently a measurement was performed at this laboratory of the excitation function of elastically scattered protons on ^{12}C for proton energies in the region of 14.230 MeV [24]. The resonance which is observed at 14.233 MeV is very sharp - at most 2 kev wide - and allows a calibration of the magnetic field of the beam preparation magnet in terms of the energy of the incoming beam. The resonance has been measured previously [25] and the energy at which it occurs is known to within 10 kev. Thus, this measurement allows a more accurate determination of the energy of the incoming beam.

The excitation energies of the levels in ^{207}Pb with the exception of the $h_{9/2}$ level are known to better than 1 kev from the beta decay of ^{207}Bi [4]. In order to determine the Q-value of the ground state and the excitation energy of the $h_{9/2}$ the Q-values and hence the excitation energies of all levels were measured. The determination of the excitation energies known from beta decay served as a check upon the method used. First, it was determined where the optic axis of the first reaction products magnet crosses the spark chamber. Then each peak was shifted to this point on the spark chamber and the magnetic field setting to center each peak was then used to determine the Q-values and excitation energies. This was done at 15 MeV, where the position of a peak is most sensitive to a change in the magnetic field and the highest accuracy could therefore be obtained. The position of the peak

could be determined to 5 kev, but the uncertainty in the determination of the absolute energy increased the uncertainty in the measurement to 0.4 %.

The target angle to be used was determined by considering the energy losses of the deuterons and the tritons. The thickness of the target is an important factor in determining the resolution that can be obtained with a magnetic analysis system. By proper choice of target angle with respect to the deuteron beam a considerable improvement can be realized. This optimum angle is computed on the assumption that the target is uniform and subject to the condition that the sum of the energy loss of the deuteron and the energy loss of the emerging triton is constant and independent of the position in the target at which the reaction occurs. This optimum angle is plotted as a function of θ, the angle of the emerging triton, in Figure 6. From the graph it is evident that a target angle of 50° is within 5° of the optimum angle for θ between 20° and 90°. The target was therefore set at this angle and was not changed during the measurement of an angular distribution.

5. DIFFERENTIAL CROSS-SECTION

The differential cross-section for a transition from the ground state of the target nucleus to a state of the final nucleus at an angle θ in the laboratory system is

$$\left(\frac{d\sigma(\theta)}{d\Omega}\right)_L = \frac{dN}{N\, n\, d\Omega}$$

where N is the number of deuterons incident, dN is the number of tritons measured at the angle θ in the solid angle $d\Omega$, and n is the

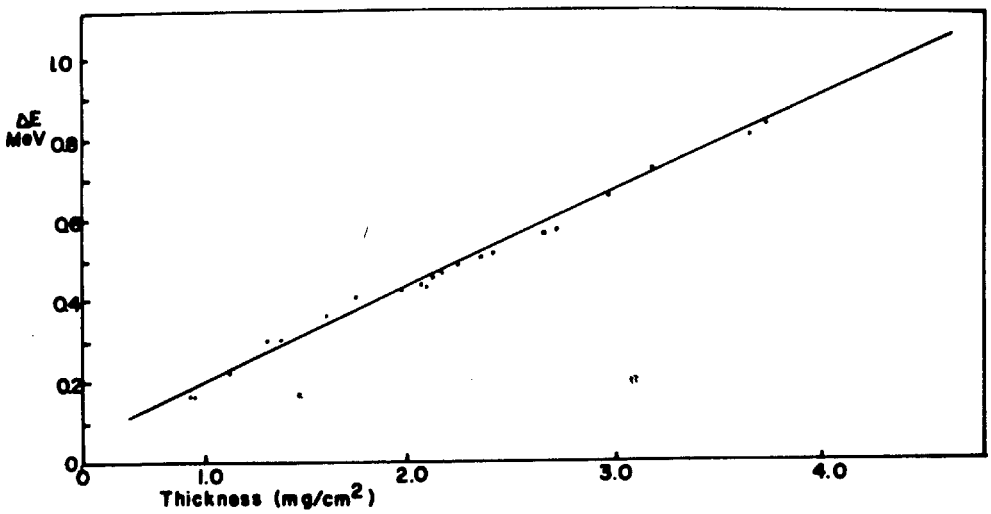

FIGURE 2 - Energy Loss of 5.48 MeV α-particles in Lead Foils (Line represents calculations [3])

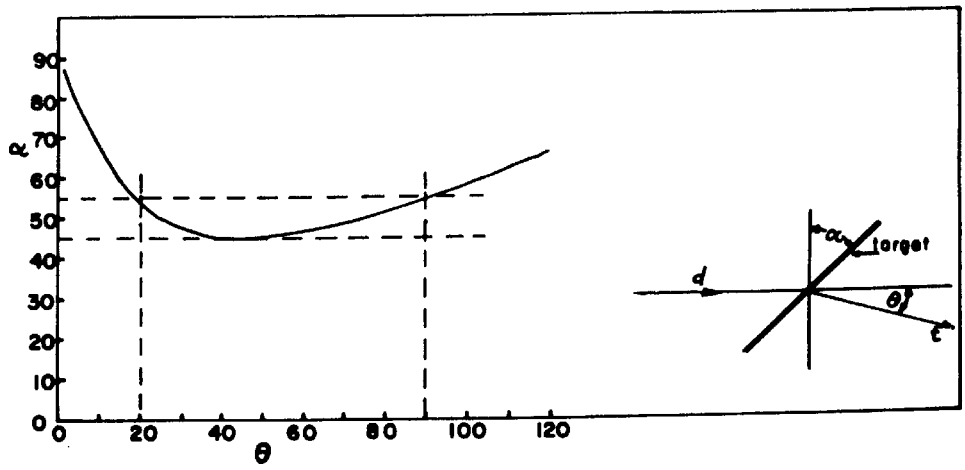

FIGURE 6 - Target Angle for Maximum Resolution for (d,t) Reaction on Lead

number of atoms of Pb^{208}/cm^2 in the target. The relation between the differential cross-section in the laboratory and center-of-mass system is well-known [6] and is

$$\left(\frac{d\sigma(\theta)}{d\Omega}\right)_{CM} = \left(\frac{d\sigma(\theta)}{d\Omega}\right)_{L} \frac{1}{E_3} \left(\frac{M_1 M_2 M_3 M_4}{(M_1 + M_2)^2 (M_3 + M_4)^2} E_1 \alpha \right)^{\frac{1}{2}}$$

$$\cdot \left(\frac{M_2 M_4}{M_1 M_3} \frac{1}{E_1} \alpha - \sin^2 \theta \right)^{\frac{1}{2}}$$

where $\alpha = E_1 + Q(1 + M_1/M_2)$

M_1, E_1 are the mass and energy of incoming particle,

M_2 is the mass of target nucleus,

M_3, E_3 are the mass and energy of outgoing particle,

M_4 is the mass of residual nucleus.

For elastic scattering this simplifies to

$$\left(\frac{d\sigma(\theta)}{d\Omega}\right)_{CM} = \left(\frac{d\sigma(\theta)}{d\Omega}\right)_{L} \cdot \frac{M_1 M_2}{(M_1 + M_2)^2} \frac{E_1}{E_3} \left(\frac{M_2}{M_1}^2 - \sin^2 \theta \right)^{\frac{1}{2}}$$

CHAPTER III

THEORY

1. SHELL MODEL

The Shell model [7] has been used successfully to explain many features of the nucleus. It treats the particles as moving in a central potential well due to the average effect of the other nucleons and in a first approximation neglects all nucleon-nucleon interactions. Two simple central potentials are the square well and the harmonic oscillator; for both the eigenfunctions and energy levels are well-known. Both potentials result in a grouping of energy levels, in the square well the higher angular momentum levels are depressed with respect to the harmonic oscillator levels. The grouping for the harmonic oscillator potential is as follows: 1s ; 1p ; 2s,1d ; 2p,1f ; 3s ; 2d,1g ; 3p,2f,1h ; 4s,3d,2g,1i . These levels are filled according to the Pauli exclusion principle. The grouping leads to the "magic numbers" 2, 8, 20, 40, 70, 112, 168. This structure agrees with experiments for the three lowest shells only, to overcome the discrepancy for the higher energy levels a spin-orbit coupling term has to be introduced into the shell model Hamiltonian:

$$H = H_o + H_{so} \tag{1}$$

where

$$H_o = \frac{p^2}{2M} + V(r) \tag{2}$$

and

$$H_{so} = V_{so}(r) \cdot \underline{\ell} \cdot \underline{s} \tag{3}$$

V(r) is the single particle potential, $V_{so}(r)$ is an average potential, the strength of which is adjusted empirically. The spin-orbit term introduces a level splitting depressing the levels with $j = \ell + \frac{1}{2}$ and raising the levels with $j = \ell - \frac{1}{2}$. To see this consider the product $(\underline{\ell} \cdot \underline{s})$.

From

$$j^2 = \ell^2 + s^2 + 2\underline{\ell} \cdot \underline{s} \tag{4}$$

it follows that

$$\underline{\ell} \cdot \underline{s} = \tfrac{1}{2}[j(j+1) - \ell(\ell+1) - 3/4]. \tag{5}$$

Substituting eq. (5) into eq. (3) results in the eigenvalues

$$E = -V_{so}(+\ell) \qquad \text{for } j = \ell + \tfrac{1}{2} \tag{6}$$

$$E = -V_{so}[-(\ell+1)] \quad \text{for } j = \ell - \tfrac{1}{2} \tag{7}$$

It is seen that splitting increases with increasing ℓ value. For the first 20 protons or neutrons this splitting does not disturb the levels enough to change the shell structure; above 20 however, some of

the levels are depressed into the next shell and this fact causes the "magic numbers" to be changed to the experimentally observed set, namely 2, 8, 20, 50, 82, 126, 184. This level scheme is represented schematically in Figure 7.

2. ^{208}PB(D,T)^{207}PB AND THE SHELL MODEL

In ^{208}Pb there are 82 protons and 126 neutrons, thus filling a shell for both the protons and the neutrons. In the (d,t) reaction on ^{208}Pb a neutron is picked out of the highest filled shell. Since the ground state of ^{208}Pb has an angular momentum of J = 0, the angular momentum transferred is simply that of the picked-up neutron. Thus the order of levels excited is expected to be: $p_{1/2}$, $f_{5/2}$, $p_{3/2}$, $i_{13/2}$, $f_{7/2}$, $h_{9/2}$, corresponding to the excited levels in ^{207}Pb. Presumably, all these levels can be well described as single particle hole states since no interference is to be expected from low-lying closed proton shells.

3. TRANSITION AMPLITUDE

Nuclear reactions are generally divided into two broad categories: direct reactions and compound reactions. In the compound reaction the incoming particle is absorbed by the target nucleus, the two form the compound nucleus and after a time long enough for the compound nucleus to "forget" how it was formed it decays into a residual nucleus and an outgoing particle. This system is difficult to describe quantum-mechanically. In the direct reactions [8, 11, 12] on the other hand, the transition from the incoming channel to the outgoing reaction channel takes place without the formation of a compound nucleus. The time of

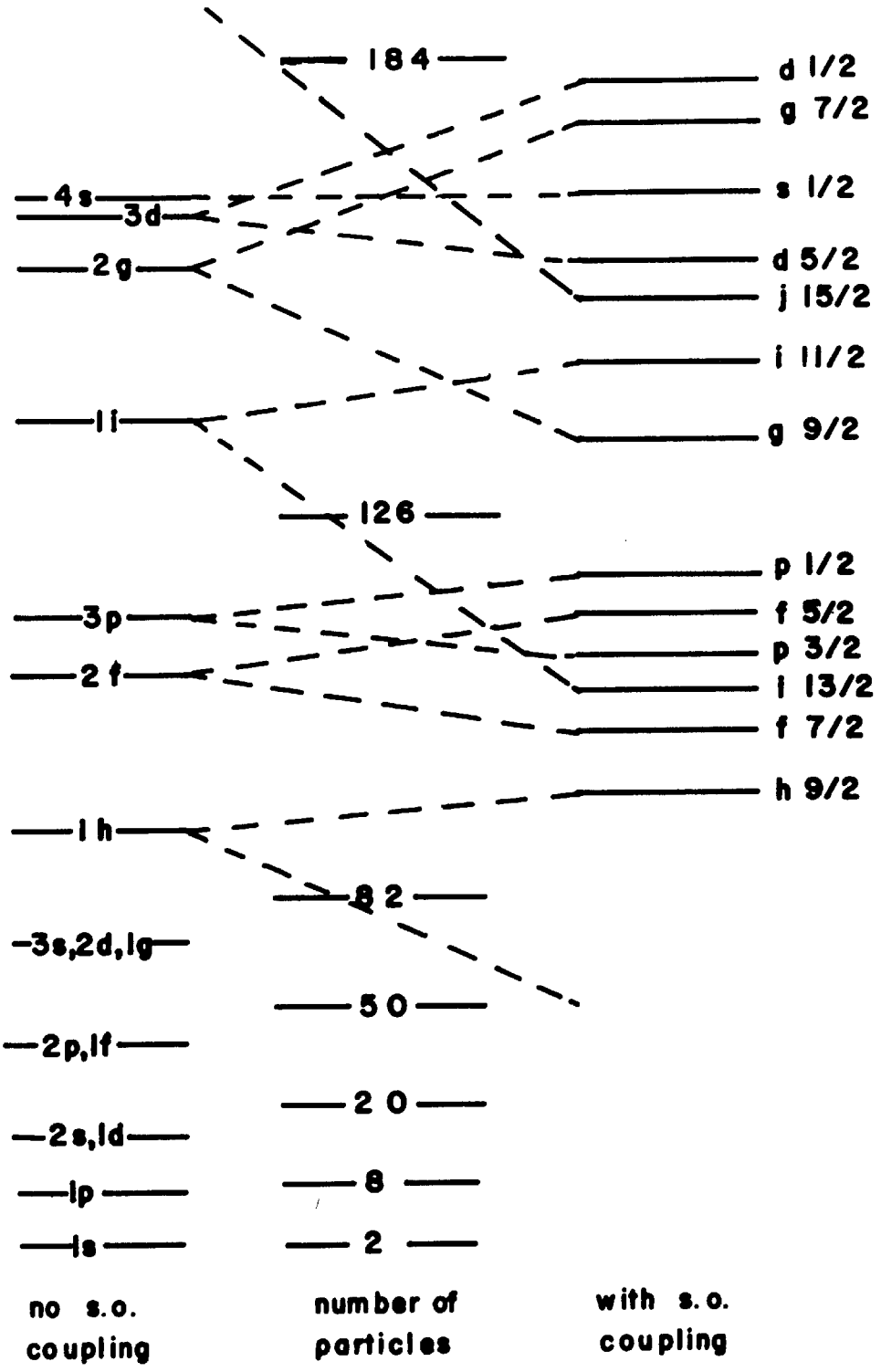

FIGURE 7 - Level Diagram

the nuclear event is comparable to the time that it takes the bombarding particle to cross the nucleus. There is good overlap between the wave functions in the incoming and outgoing channels, so that the reaction may proceed with a minimum of rearrangement taking place within the target nucleus.

The best example of a direct reaction is elastic scattering, where the wave functions in the incoming and outgoing channel are identical. The elastic scattering reaction is frequently described by the optical model, in which the interaction potential is assumed to consist of the coulomb potential and a Wood-Saxon type nuclear potential. The Schroedinger equation describing the interaction is solved by using a partial wave expansion in the wave function. The solution is a "distorted wave" consisting of an incoming wave and an outgoing wave due to the nuclear and coulomb potential.

In the analysis of a rearrangement collision the optical model solution is used as a first approximation and perturbations are introduced which account for the inelastic events. These perturbations are introduced through an interaction potential. The target nucleus is usually regarded as consisting of a core and a nuclide in a bound state. The potential considered responsible for the inelastic or rearrangement event is the one between the bombarding nucleus and the target nuclide, all other potentials are considered to be negligible. This approach is used in the distorted wave Born approximation (DWBA) in which the relative motion of the nuclei involved in the interaction before and after the collision is described by distorted waves.

It should always be kept in mind that this is an oversimplifica-

tion of the real process and a model only. However, it has proven useful in nuclear spectroscopy.

In a direct reaction of the form A(a,b) B the Hamiltonian may be written as

$$H = H_\alpha + V_\alpha + T_\alpha \tag{8}$$

$$= H_\beta + V_\beta + T_\beta \tag{9}$$

where α and β stand for the system before and after the collision. The Schroedinger equation for the whole system is

$$(E - H)\,\Psi = 0 \tag{10}$$

and for the internal states of each pair the following relations hold

$$(E_\alpha - H_\alpha)\,\Psi_\alpha = 0, \qquad (E_\beta - H_\beta)\,\Psi_\beta = 0 \tag{11}$$

E_α, E_β are related to E by

$$E = E_\alpha + \frac{\hbar^2 k_\alpha^2}{2m_\alpha} = E_\beta + \frac{\hbar^2 k_\beta^2}{2m_\beta} \tag{12}$$

where $\hbar\, k_\alpha$ gives the relative momentum of a with respect to A and m_α is the reduced mass in channel α.

The transition amplitude is given exactly by [12]

$$T = \langle \psi_\beta \, | V_\beta | \, \Psi_\alpha^{(+)} \rangle \qquad (13)$$

where Ψ_α represents an incoming wave in channel α and outgoing waves in all channels. Only the post-interaction form is given and it will be used from now on; the prior-interaction form could be used as well, it would lead to a different - but equally valid - approximation.

The problem that arises is to find a form of Ψ_α that makes it possible to calculate the transition amplitude without making unreasonable assumptions. In the DWB approximation the fact that the elastic scattering is the most important process in most cases is made use of and contributions to the transition amplitude arising from parts in Ψ_α other than the elastic, such as the inelastic scattering and rearrangement contributions, are neglected. This assumption does not cause any problems in the regions which are far from the target nucleus. In the regions where the projectile and the target interact strongly, and particularly inside the nucleus there is no guarantee that this choice of the wave function is reasonable. The uncertainty introduced depends upon the relative contributions to the matrix element from the interior and exterior region; the closer to the surface the interaction takes place, the better the agreement should be with experiment.

In detail the transition amplitude in the DWB approximation has the form

$$T = J \int d\underline{r}_a \int dr_b \, \chi_b^{(-)} (\underline{k}_b, \underline{r}_b) < B, b \, |V_{int}| \, A, a >$$

$$\cdot \chi_a^{(+)} (\underline{k}_a, \underline{r}_a) \qquad (14)$$

and r_a and r_b are the distances of a from A and of b from B respectively. χ_a and χ_b are the optical model distorted waves, obtained from elastic scattering data, and B, b, A, and a refer to the internal states. J is the Jacobian of the transformation to the relative coordinates $\underline{r}_a$ and $\underline{r}_b$. (For a derivation of this expression see Reference 11). The Transition amplitude is the integral of the interaction potential, V_{int}, taken between wave function describing the system before the collision and the wave function describing the system after the collision. Either wave function consists of a product of the wave functions describing 1) the internal motion of the target or residual nucleus, A or B, and 2) the internal motion of the projectile, a or b, and 3) the relative motion of the projectile with respect to the target, namely, the distorted waves, χ_a and χ_b.

4. DISTORTED WAVES

The distorted waves are obtained from optical model analysis [8, 10]. A charged incident particle is scattered by the nuclear potential, U, and the coulomb potential V_c which differs from a point charge potential at close distances. The Schroedinger equation in this case is

$$\left[\frac{\hbar^2}{2\mu} \nabla^2 + U(r) + V_c(r) \right] \chi = E \chi \qquad (15)$$

The partial wave expansion of χ is

$$\chi = 4\pi \sum_{\ell m} i^{\ell} e^{i\sigma_\ell} \frac{\varphi_\ell(k, r)}{kr} Y_\ell^{m*}(\underline{k}) Y_\ell^m(\underline{r}) \qquad (16)$$

The partial waves $\varphi_\ell(k, r)$ must satisfy the radial equation

$$\left[-\frac{d^2}{dr^2} + \ell(\ell+1) \cdot \frac{1}{r^2} + \frac{2\mu}{\hbar^2} (U(r) + V_c(r)) \right] \varphi_\ell(k, r) =$$

$$k^2 \varphi_\ell(k, r) \qquad (17)$$

The solution to this equation must reduce to the familiar form of pure coulomb scattering when the potentials are reduced to a coulomb point charge potential. In the asymptotic form φ_ℓ becomes

$$\varphi_\ell \tilde{=} \mathcal{F}_\ell(\eta, kr) + C_\ell [G_\ell(\eta, kr) + i \mathcal{F}_\ell(\eta, kr)] \qquad (18)$$

$$\tilde{=} \sin \theta_\ell + C_\ell e^{i\theta_\ell} \qquad (19)$$

where

$$\theta_\ell = kr - \eta \ln 2kr - \ell\pi/2 + \sigma_\ell \qquad (20)$$

σ_ℓ is the usual coulomb phase shift and η the coulomb parameter. The first term in eq. (19) is the asymptotic form of F_ℓ, the regular coulomb function; the second term represents the contribution of the nuclear potential in the outgoing wave.

In the optical model analysis eq. (17) is integrated numerically and the wave function is matched to eq. (19) at a radius where the nuclear potential is negligible. For each partial wave a C_ℓ is calculated, which is related to the nuclear phaseshift by

$$C_\ell = \frac{1}{2i}\left[e^{2i\delta_\ell} - 1\right] \tag{21}$$

After substituting eq. (19) into the distorted wave equation (16) the asymptotic form of the distorted waves can be written in the form

$$\chi = f_c + \frac{1}{k}\sum_\ell (2\ell + 1)\, e^{2i\sigma_\ell} C_\ell P_\ell (\cos\theta) \cdot \frac{e^{i(kr - \eta \ln 2kr)}}{r} \tag{22}$$

where f_c is the coulomb scattering wave function which is the solution to the Schroedinger equation

$$-\frac{\hbar^2}{2\mu}\nabla^2 f_c + \frac{ZZ'e^2}{r} f_c = Ef_c \tag{23}$$

Thus the distorted wave has been divided into an incoming wave with the normal coulomb scattering effect included and an outgoing wave which is due to the nuclear potential and also includes non-local effects of the coulomb potential.

The nuclear potential used is of the Woods-Saxon shape and has a real part, V, and an imaginary part, W, i.e.,

$$V(r) = -V_o(1 + e^x)^{-1} \tag{24}$$

$$W(r) = -W_o(1 + e^{x'})^{-1} - W_D e^{x'}(1 + e^{x'})^{-2} \tag{25}$$

where

$$x = (r - R_o A^{1/3})/\underline{a} \tag{26}$$

$$x' = (r - R_o' A^{1/3})/\underline{a}' \tag{27}$$

V_o and W_o are respectively the real and imaginary part of the nuclear potential, R_o is the nuclear radius constant and $\underline{a}$ and $\underline{a}'$ are the diffuseness parameters. The second term in W(r) is the derivative of the Woods-Saxon potential and this term is responsible for the surface absorption.

For the coulomb potential uniform charge distribution is assumed inside the nucleus

$$V_c = (ZZ'e^2/2R_c)\ (3 - r^2/R_c^2) \qquad \text{for } r < R_c \tag{28}$$

$$= ZZ'\ e^2/r \qquad \text{for } r > R_c \tag{29}$$

5. NUCLEAR MATRIX ELEMENT

The important factor in the transition amplitude is the matrix

element [9] of the interaction potential taken between the internal states of the nuclei involved in the collision, namely

$$< B, b \,|V_{int}|\, A, a > . \qquad (30)$$

This matrix element contains all the information about nuclear structure and about the reaction considered; it represents the interaction for the transition from one elastic scattering state, χ_a, to another, χ_b.

In discussing the nuclear matrix, only stripping reactions in which the transferred particle is a neutron will be considered; pick-up reactions such as the (d,t) are just the inverse process and are related to the stripping reaction by the theorem of detailed balance which will be discussed in a later section. In a reaction of the form A(a,b) B it is assumed that a is made up of two parts, namely, b and the transferred particle n, i.e., a = b + n. The angular momentum transferred in the reaction is j, consisting of orbital momentum ℓ and a spin part s. The angular momentum of the target and residual nucleus is J_A and J_B respectively, the bombarding particle has spin s_a and the emitted particle spin s_b. Between these quantities the following relations hold

$$\underline{j} = \underline{J}_A - \underline{J}_B, \quad \underline{s} = \underline{s}_a - \underline{s}_b, \quad \underline{j} = \underline{\ell} + \underline{s} \qquad (31)$$

In determing the form V_{int} it is useful to think of the residual nucleus B as made up of the target nucleus plus a bound neutron. The major potential is V_{bn}, which becomes particularly obvious when one

considers the inverse, namely the pick-up of n by b. The two potentials V_{bB} and V_{bA} are also part of V_{int}, but their contribution to the matrix is generally thought to be small. Furthermore, their contributions should cancel out to a large degree. It thus seems to be a good approximation to neglect all potentials except V_{bn}. This allows us to rewrite equation (30) in the following manner

$$<B,\ b\ |V_{bn}|A,\ a> = <\ B\ |A><\ b|V_{bn}|\ a>. \tag{32}$$

As we said before, the nucleus B is considered as consisting of nucleus A with a bound neutron, therefore, the wave function of B, ψ_B, can be written as the wave function for the bound neutron, $\phi_{j\mu}$, coupled to the wave function of A, ψ_A.

$$< B|A > = \int \psi_B^* (\xi_A, \xi_n\ r_{nA})\ \psi_A(\xi_A)\ d\xi_A \tag{33}$$

$$= \sum_j < J_A j\ M_A\mu | J_B M_B > \phi^*_{j\mu}\ (\xi_n, r_{nA}) \tag{34}$$

where ξ_A are the internal coordinates of A and ξ_n is the neutron spin variable. The Clebsch-Gordon coefficient gives the angular momentum coupling of the neutron to the core A. $\phi_{j\mu}$ can be expanded again

$$\phi_{j\mu}(\xi_n, r_{nA}) = \sum_m < \ell\ \tfrac{1}{2} m\ \mu - m | j\mu > R_{\ell j}(r_n)\ i^\ell Y_\ell^m\ (\theta_n \phi_n)\ \psi_{\frac{1}{2}\ \mu-m}(\xi_n)$$

(35)

$\emptyset$ is taken to be proportional to the shell model single-particle wave function, so that the radial part $R_j(r_n)$ can be written

$$R_{\ell j}(r_n) = \sqrt{S_{\ell j}}\, u_{n\ell j}(r), \tag{36}$$

where $u_{n\ell j}(r)$ is the normalized radial wave function and $S_{\ell j}$ is the spectroscopic factor [13]. The shell model single particle wave functions are determined by solving the Schroedinger equation

$$(T + V)\, u_{n\ell j}(r) = - B_n\, u_{n\ell j}(r) \tag{37}$$

where B_n is the binding energy and V is taken to be of the form

$$V = - V_o \frac{1}{(1 + e^x)} - \ell\lambda V_o \frac{e^{x'}}{(1 + e^{x'})^2} \qquad \text{for } j = \ell + \tfrac{1}{2} \tag{38}$$

$$V = - V_o \frac{1}{(1 + e^x)} + (\ell + 1)\, \lambda V_o \frac{e^{x'}}{(1 + e^{x'})^2} \qquad \text{for } j = \ell - \tfrac{1}{2} \tag{39}$$

where

$$x = (r - R_o A^{1/3})/a \tag{40}$$

The depth of the potential well is adjusted to give the correct binding energy.

The remaining factor in equation (32), namely

$$< b|V_{bn}| a > \tag{41}$$

consists of the interaction potential and the wave functions of the incoming and outgoing particle. For the deuteron, the D-state contribution is usually neglected, the deuteron wave function can then be written as

$$\phi_d(\xi_p, \xi_n, r_{pn}) = \phi_d(r_{pn}) \cdot \psi_{1m_d}(\xi_d) \tag{42}$$

where ψ is the spin part and where usually the Hulthen wave function is used for the radial part, i.e.,

$$\phi_d(r_{pn}) = \sqrt{\frac{\alpha\beta(\alpha + \beta)}{2\pi(\alpha - \beta)^2}} \; \frac{e^{-\alpha r} - e^{-\beta r}}{r} \tag{43}$$

α is related to the deuteron binding energy, ϵ, by

$$\epsilon = \hbar^2 \alpha^2 / M \tag{44}$$

The internal motion of the triton can be described by

$$\phi_{\frac{1}{2} m_T}(\xi_T) = \phi_T \sum_{m_d} < \tfrac{1}{2}\, 1 (m_T - m_d)\, m_d | \tfrac{1}{2}\, m_T > \psi_{\frac{1}{2}\, m_T - m_d}(\xi_n)\, \psi_{1m_d}(\xi_d). \tag{45}$$

ϕ_T is best described by the Irving-Gunn wave function [14, 15]

$$\phi_T(r_1 r_2 r_3) = A \frac{\exp(-\delta R/2)}{R} \tag{46}$$

where

$$R^2 = \sum_{i<j} (r_{ij})^2$$

Now, considering only an A(t,d) B reaction, equations (34), (35), (42) and (45) are substituted into the nuclear matrix element

$$\langle B, d | V_{dn} | At \rangle = \sum \langle J_A j M_A \mu | J_B M_B \rangle \langle \ell \tfrac{1}{2} m \mu - m | j \mu \rangle \tag{47}$$

$$\cdot \langle 1 \tfrac{1}{2} m_d (m_T - m_d) | \tfrac{1}{2} m_T \rangle R_{\ell j}(r_{nA}) \left[i^{\ell} Y^m(\theta_n \phi_n) \right]^*$$

$$\cdot \int V_{dn} \phi_d(r_{pn}) \phi_T(r_1 r_2 r_3) \, dr$$

$$\cdot \int \psi^*_{\frac{1}{2} \mu - m}(\xi_n) \psi^*_{1 m_d}(\xi_d) \psi_{\frac{1}{2} m_T - m_d}(\xi_n) \psi_{1 m_d}(\xi_d) \, d\xi_n d\xi_d$$

The integral over the spin wave functions is equal to one; for convenience a quantity $D(r_{dn})$ is defined

$$D(r_{dn}) = C_{dn} J \int V_{dn}(r_{dn}) \phi_d(r_d) \phi_T(r_{dn}, r_d) \, dr_d \tag{48}$$

where ϕ_T has been transformed to the relative coordinates r_{dn} and r_d, resulting in a Jacobian, J, and where C_{dn} is the coefficient of fractional parentage for decomposing the triton into the deuteron n-p pair and the extra neutron. This expression simplifies still further in making the zero-range approximation, i.e., the interaction is assumed to be of zero range which implies that the outgoing particle is emitted where the incoming particle is absorbed. For this approximation to be good either the potential or one of the internal wave function must be of short range. Then

$$D(r_{dn}) \tilde{=} D_o \, \delta(r_{dn}) \tag{49}$$

where D_o can be calculated directly [15].

6. CROSS-SECTION

Once the transition amplitude is known, the differential cross-section is given by

$$\frac{d\sigma}{d\Omega} = \frac{m_\alpha m_\beta}{\left(2\pi\hbar^2\right)^2} \frac{k_d}{k_t} \frac{\sum |T|^2}{(2J_A + 1)\ (2s_t + 1)} \tag{50}$$

where m_α and m_β are reduced masses. The sum is over all M_A, M_B, m_T and m_d. Eq. (50) is seen to be the sum over all final states and the average over all initial states. This sum can be carried out, making use of the orthogonality of the Clebsch-Gordon coefficients in equation (47) which removes interference between different j, ℓ and s values. The

sum eliminates the Clebsch-Gòrdon coefficients and introduces a factor because of the orthogonality relation

$$\sum_{M_A, M_B} \left[< J_A j \; M_A \mu | J_B M_B > \right]^2 = \frac{2J_B + 1}{2j + 1} \tag{51}$$

The cross-section can now be written in the convenient form

$$\frac{d\sigma}{d\Omega} = \frac{(2J_B + 1)}{(2J_A + 1)} \sum_j S_{\ell j} \, D_o^2 \cdot \frac{d\sigma}{d\Omega}_{\text{calc.}} \tag{54}$$

where certain convenient factors have been stated explicitly, all other terms are included in $\frac{d\sigma}{d\Omega}_{\text{calc.}}$, which is calculated with the aid of a computer.

7. INVERSE REACTION

The stripping reaction is related to its inverse, the pick-up reaction, by the theorem of detailed balance [16] which states that

$$\frac{d\sigma}{d\Omega}_{\text{pick up}} = \frac{(2J_t + 1)\ (2J_A + 1)}{(2J_d + 1)\ (2J_B + 1)} \quad \frac{k_t^2}{k_d^2} \; \frac{d\sigma}{d\Omega}_{\text{stripping}} \tag{55}$$

and since $\frac{d\sigma}{d\Omega}_{\text{stripping}}$ contains a factor (see eq. (50) and (54))

$$\frac{(2J_B + 1)}{(2J_A + 1)} \quad \frac{k_d}{k_t} ,$$

this term only has to be replaced by

$$\frac{(2J_t + 1)}{(2J_d + 1)} \quad \frac{k_t}{k_d}$$

to effect the change over. In going from the (t,d) reaction to the (d,t) reaction this term simplifies to

$$\frac{2}{3} \quad \frac{k_t}{k_d} .$$

CHAPTER IV

RESULTS AND DISCUSSION

1. THE SPECTRUM

In the (d,t) reaction on ^{208}Pb eight levels have been found up to an excitation energy of 3.6 MeV, five of which are well established single particle levels, namely the $p_{1/2}$, $f_{5/2}$, $p_{3/2}$, $i_{13/2}$, $f_{7/2}$. Between 3.2 and 3.6 MeV four weak levels have been observed, the strongest (100 μb/str) of which was identified as the $h_{9/2}$ single particle level. The three others never exceeded 10 μb/str in cross-section.

Typical spectra obtained for a deuteron energy of 24.8 MeV and at a scattering angle of 25° are shown in Figure 8. In the spectrum shown in the upper part of Figure 8 the tritons were recorded in nuclear emulsion, while in the spectrum shown in the lower half of the figure the tritons were recorded with the spark chamber.

The background is seen to be very low and there are no contributions from contaminants such as oxygen and carbon. The spectra shown as well as all other data were taken with a target prepared from lead enriched to 99.3 % in ^{208}Pb. The contributions from other Pb isotopes are therefore negligible.

The spark chamber spectrum was plotted directly from the multichannel analyser using an x-y plotter. The unit of the abscissa, the channel number, cannot be easily and accurately calibrated in terms of energy since it is a function of the dispersion of the reaction products magnet, the speed of sound in the chamber which varies with pressure, the linearity of the time-to-pulse-height converter and the

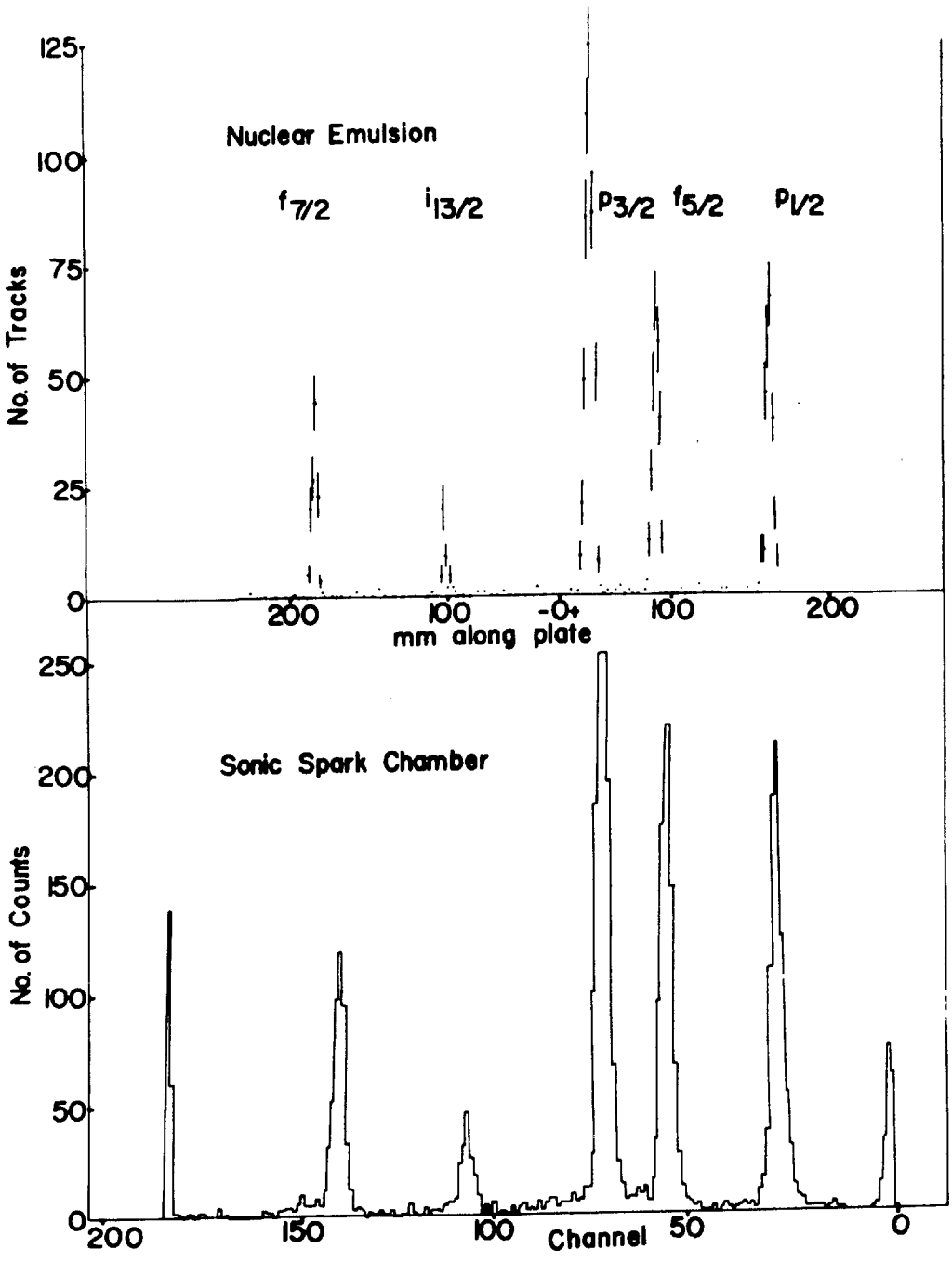

FIGURE 8 - Typical Spectra Obtained in the Reaction $^{208}Pb(d,t)^{207}Pb$ at a Deuteron Energy of 24.8 MeV

linearity of the multi-channel analyser.

The Q-value of the ground state and the excitation energies of the excited states were determined by the method described in Chapter II. The results are summarized in Table II where they are compared with values obtained elsewhere.

2. ANGULAR DISTRIBUTIONS

The differential cross-sections were measured at 14.8, 20.1, and 24.8 MeV. Each angular distribution was measured at least twice, once with the spark chamber and once with nuclear emulsions. Good agreement was found between the two methods of recording data.

The energies at which the distributions were measured were determined by the two methods described in Chapter II. The results are summarized in Table III. The two methods give results which agree within the uncertainty of the measurements; the values listed in column three are the more accurate ones however, and therefore these values have been used in discussing the results. The DWBA calculations were performed at the energies listed in column four, because at the time the calculations were performed only approximate values for the deuteron energies were available.

Figures 9 through 11 present the elastic scattering data together with the results of the optical model calculations. Only one set of parameters was used for the calculations at all three energies, the set had been determined from elastic scattering done at 25.1 MeV [17]. The parameters used are listed in Table IV.

Figures 12 through 14 show angular distributions of the $p_{1/2}$, $f_{5/2}$, $p_{3/2}$, $i_{13/2}$, $f_{7/2}$ at the three energies. Both the data and the

TABLE II

Excitation Energies and Q-Value

Level	Present Work	Brady et al.[a]	Cohen[b]	Harvey[c]
$p_{1/2}$	Q = -1.127 ± .008		-1.12	-1.10
$f_{5/2}$	0.567 ± .006	0.570	0.57	0.61
$p_{3/2}$	0.891 ± .006	0.897	0.90	0.95
$i_{13/2}$	1.640 ± .007	1.633	1.64	1.61
$f_{7/2}$	2.341 ± .008	2.339	2.35	2.33
	3.23 ± .01			
	3.33 ± .01		3.38	
$h_{9/2}$	3.43 ± .01		3.47	
	3.59 + .01			

a) see reference 4.

b) B. L. Cohen, S. Mayo, R.E. Price, Nuclear Physics, 20, 360 (1960).

c) J. A. Harvey, Can. J. Phys., 31, 278 (1953).

TABLE III

Deuteron Energies

NMR Freq. of Beam Preparation Magnet	Energies Using Elastically Scatt. Deuterons	Energies Using Proton Resonance of ^{12}C at 14.233 MeV	Energies Used in Calculations
17344 kc	14.94 ± .15 MeV	14.84 ± .04 MeV	15.0 MeV
20180	20.18 ± .20	20.07 ± .04	20.3
22432	24.91 ± .25	24.76 ± .05	25.1

TABLE IV

DWBA Parameters Used to Obtain Best Fit to Measured Distributions

Deuteron	Neutron	Triton
V_o = 100 MeV		V_o = 168 MeV
W_o = 0		W_o = see below
R_o = 1.14 fm	R_o = 1.225 fm	R_o = 1.14 fm
r_c = 1.3 fm		r_c = 1.4 fm
$\underline{a}$ = 0.89 fm	$\underline{a}$ = 0.70 fm	$\underline{a}$ = .723 fm
R_o' = 1.33 fm		R_o' = 1.52 fm
a' = 0.75 fm		a' = 0.77 fm
W_D = 13.8 MeV		W_D = 0
	λ_{eff} = 25	

W_o for triton: W_o = 17 MeV for E_d = 15 MeV
19 20.3
22 25.1

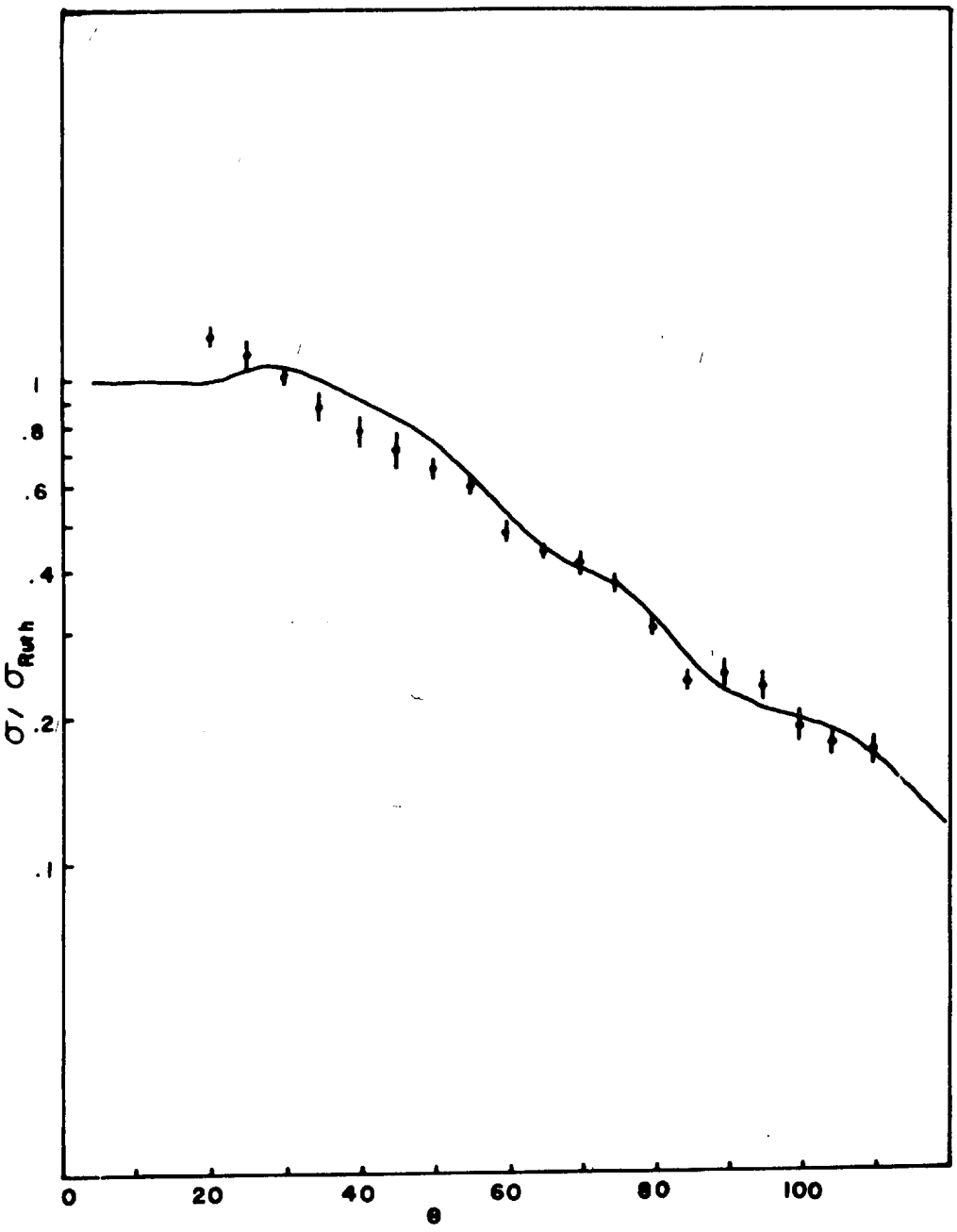

FIGURE 9 - Angular Distribution for 14.8 MeV Deuterons Elastically Scattered from ^{208}Pb

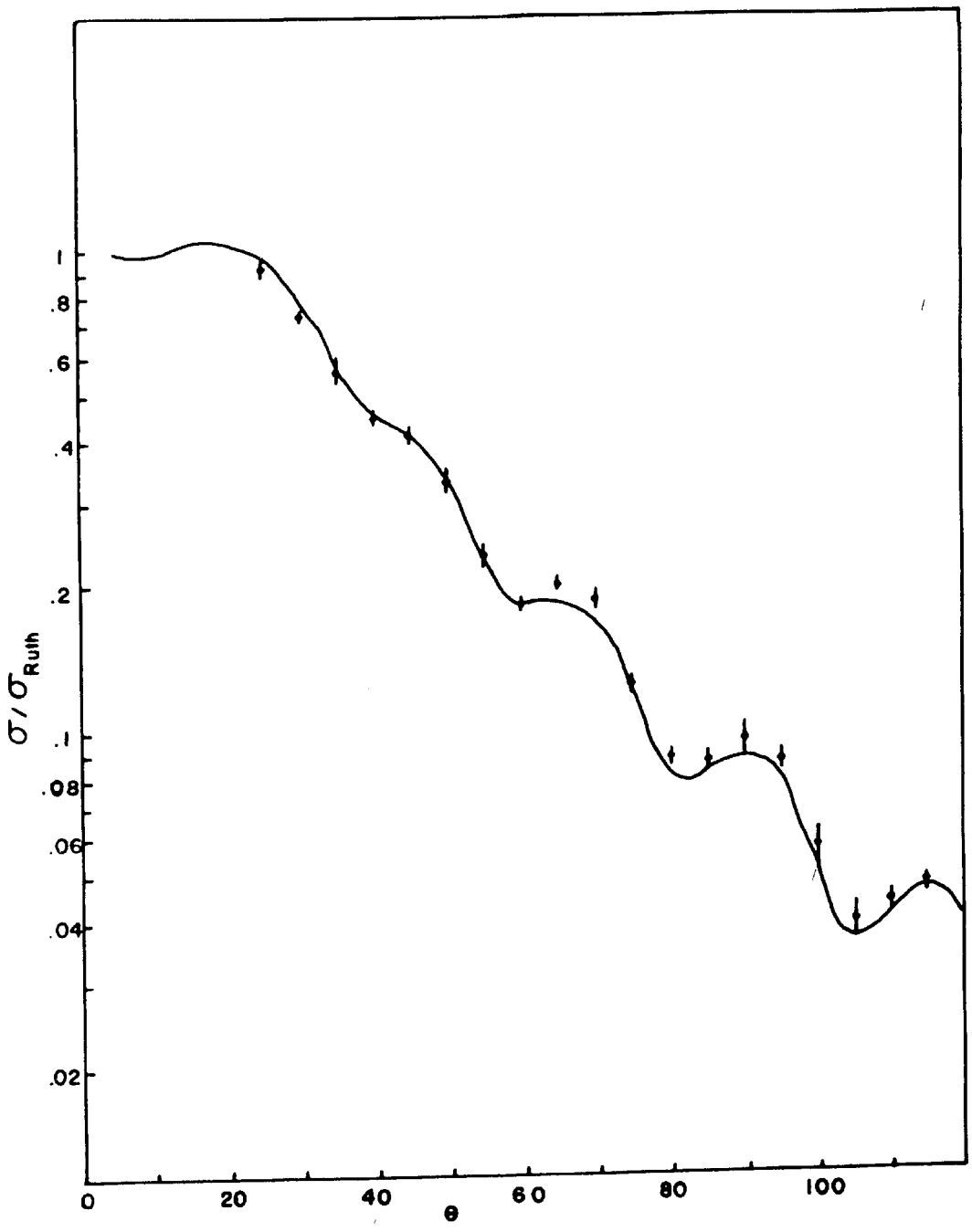

FIGURE 10 - Angular Distribution for 20.1 MeV Deuterons Elastically Scattered from ^{208}Pb

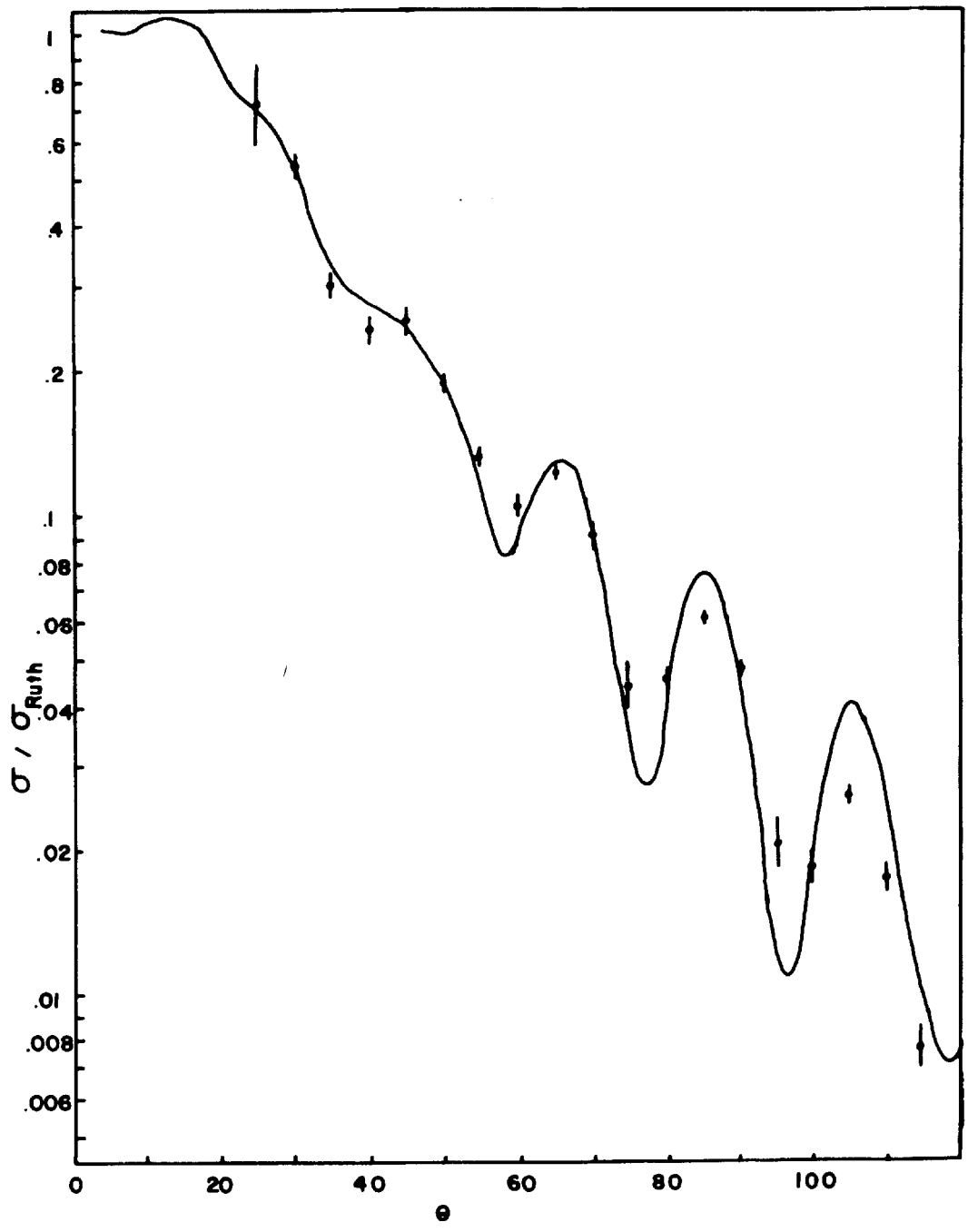

FIGURE 11 - Angular Distribution for 24.8 MeV Deuterons Elastically Scattered from ^{208}Pb

DWBA curves are shown. The parameters used in the calculations are shown in Table IV. The DWBA curves were adjusted visually to give the best fit to the data. The spectroscopic factors obtained by comparing the calculated differential cross-section to the measured differential cross-section are shown in Table V.

An angular distribution was measured at 20.1 MeV for the level at an excitation energy of 3.43 MeV and compared to a DWBA calculation for an $h_{9/2}$ level. Both the experimental results and the calculated curve are shown on an absolute scale in Figure 15. The agreement is excellent and this can be considered as quite strong evidence that this level is the $h_{9/2}$ level. In previous work [18] it was suggested that the $h_{9/2}$ level was at an excitation energy of 3.47 MeV although no conclusive measurements were made.

Looking at the angular distributions as shown in Figures 12-14 a number of interesting observations are to be made. At 14.8 MeV, an energy just above the coulomb barrier, the shape is strongly influenced by the coulomb field. All of the distributions peak near 60° and fall slightly at the back angles. The principal difference between different ℓ-transitions is the amount that the distributions fall off at the forward angles. At 20.1 MeV the distributions fall roughly a decade between 40° and 100°. The peaks have shifted toward smaller angles and fall at quite different angles for different ℓ-transitions. The p levels peak at 8°, the f levels at 25° and the i level at 40°; the peak shifts to larger angles for higher ℓ-transitions. In going from 20.1 to 24.8 MeV little is changed; the distributions are again forward peaked, the peaks have moved only a few degrees closer to zero. The fall-off at the back angles has become

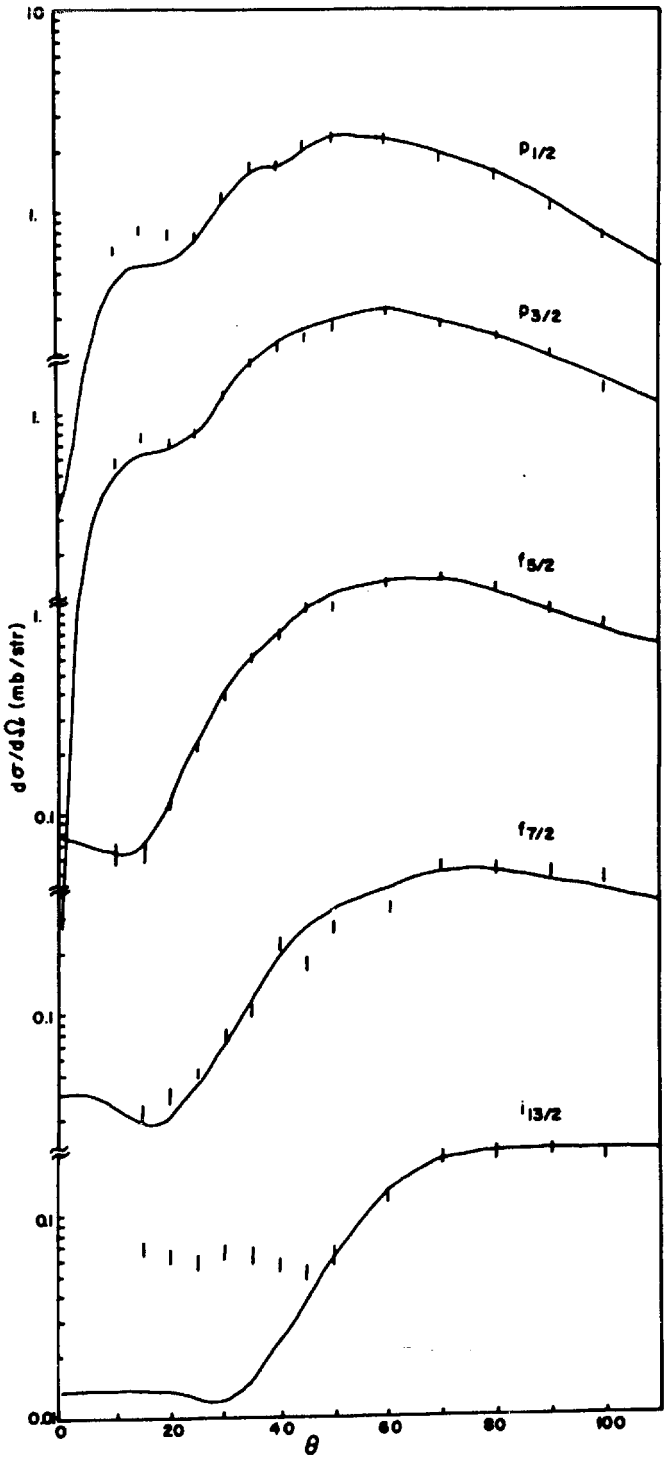

FIGURE 12 - Angular Distribution of Triton Groups in the Reaction $^{208}Pb(d,t)^{207}Pb$ at a Deuteron Energy of 14.8 MeV

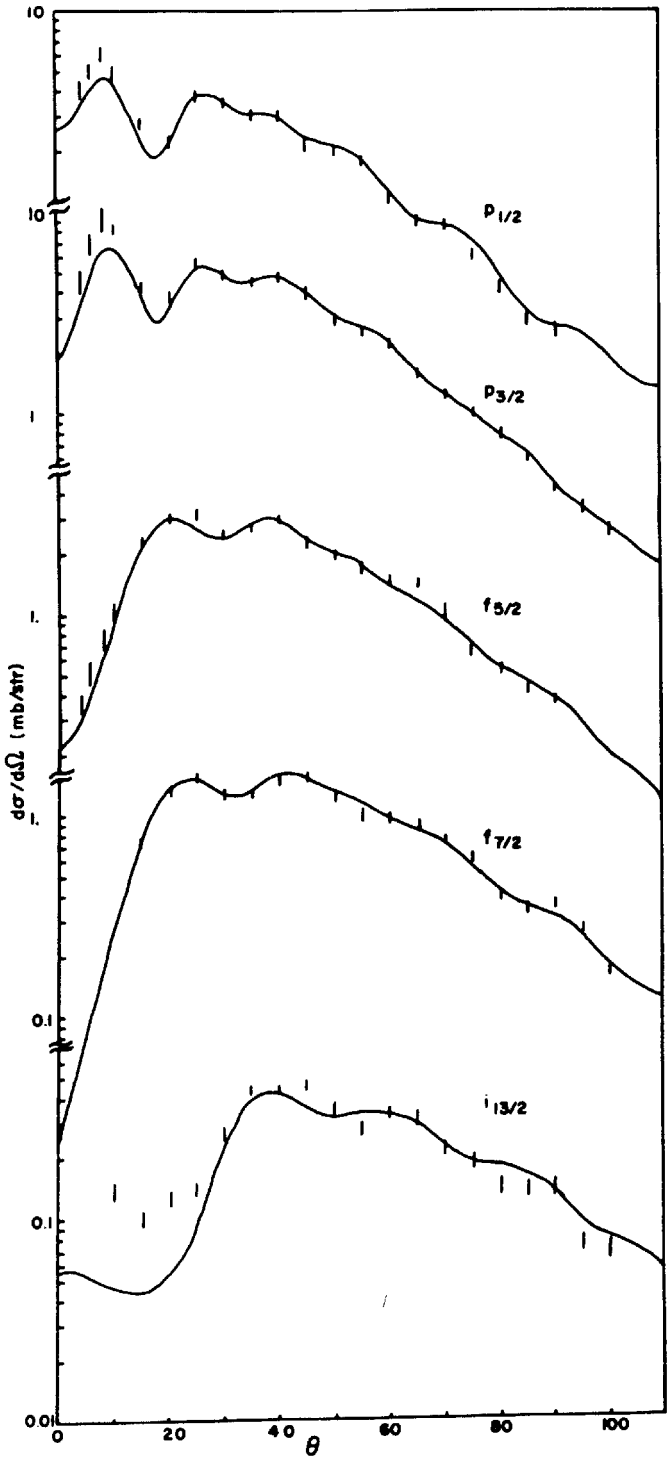

FIGURE 13 - Angular Distribution of Triton Groups in the Reaction $^{208}Pb(d,t)^{207}Pb$ at a Deuteron Energy of 20.1 MeV

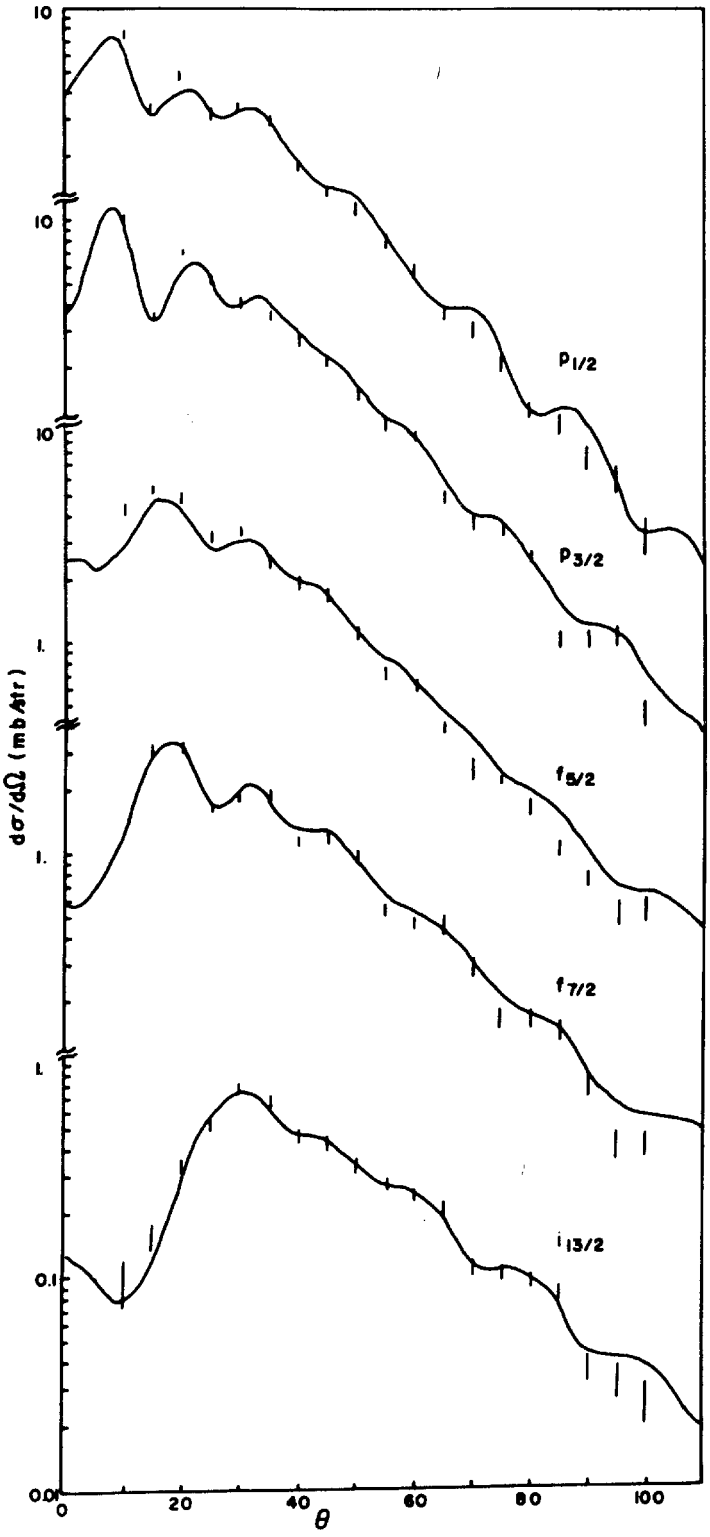

FIGURE 14 - Angular Distribution of Triton Groups in the Reaction $^{208}Pb(d,t)^{207}Pb$ at a Deuteron Energy of 24.8 MeV

TABLE V

Spectroscopic Factors

Level	14.8 MeV	20.1 MeV	24.8 MeV
$p_{1/2}$	1.09	1.06	1.06
$f_{5/2}$	1.10	1.20	1.00
$p_{3/2}$	0.94	0.95	0.83
$i_{13/2}$	1.00	0.93	1.00
$f_{7/2}$	0.76	0.80	0.72

Spectroscopic factors given by the DWBA analysis using the parameters of Table IV.

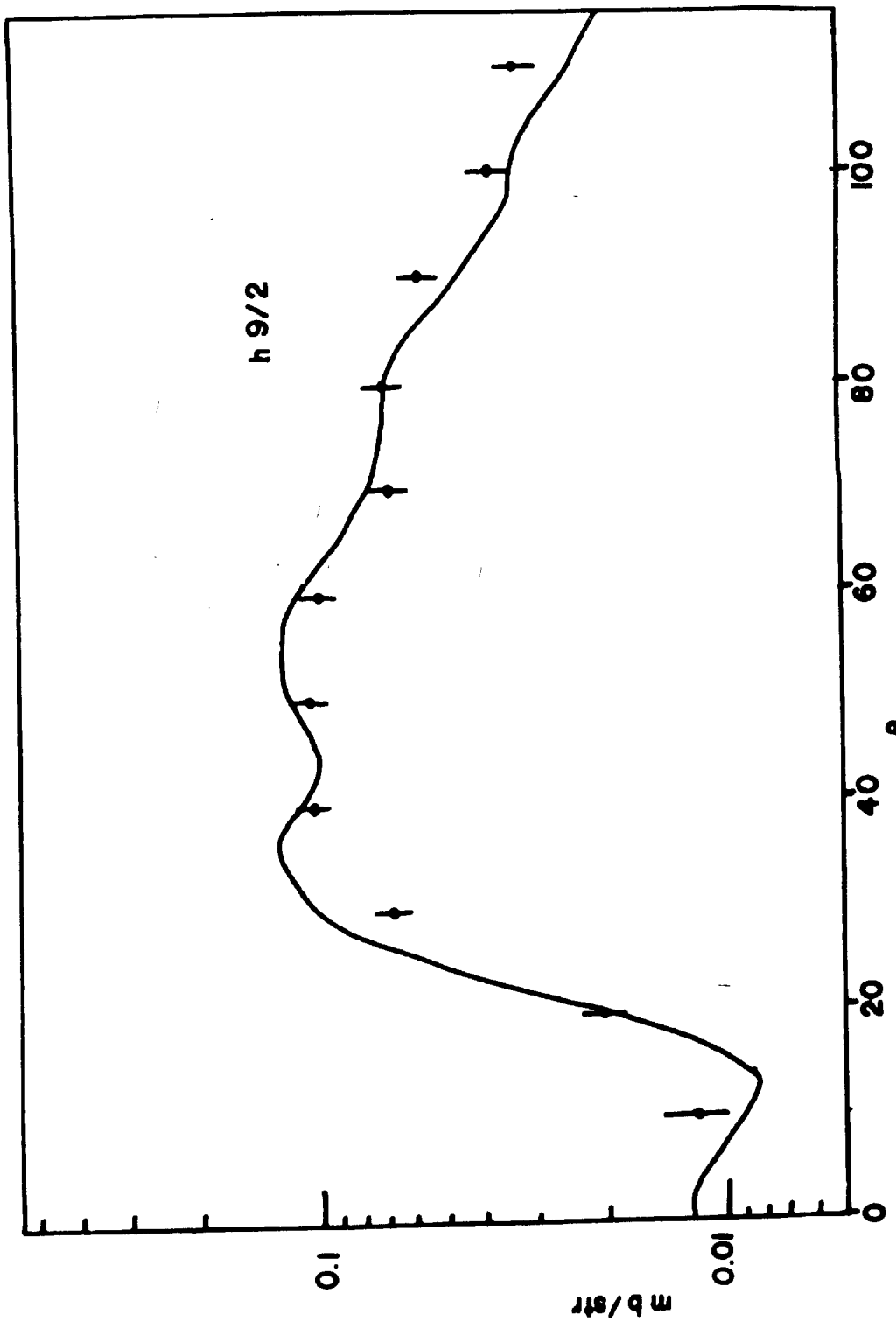

FIGURE 15 - Angular Distribution of $h_{9/2}$ at 20.1 MeV

more pronounced, most distributions fall a factor of 100 from the peak to 100°. At all three energies the distributions show rather little structure at the backward angles. The peak cross-section for all levels increases with increasing energy as is to be expected in this energy and mass region.

3. THE DWBA CALCULATIONS

The DWBA analysis can be of value for the extraction of spectroscopic information from data of the type described only if a single set of parameters can be found which accurately reproduces the data for pure single particle states and which is relatively insensitive to changes in bombarding energy, Q-value and target mass.

The parameters can be classified in two groups. The first group specifies the kinematics of the reaction, that is, the binding energy, spins and masses of particles involved. These are the "constant" factors. The second group, the "variables", fall into three categories:

A. The optical model parameters for the incoming particle, in this case the deuteron;

B. The parameters which determine the wave function of the bound neutron;

C. The optical model parameters for the outgoing particle, in this case the triton.

A. Deuteron Parameters: The deuteron parameters used in the analysis are those given in Table IV, which reproduce all elastic scattering data available over a wide range of energies. The parameters were considered known and no attempt was made to vary them.

B. Neutron Bound State Parameters: The neutron, when bound to the target nucleus, is considered to move in a shell model potential well. The potential is of the form of eq. (38),(39) and the parameters specifying it are somewhat uncertain. To determine the sensitivity of the differential cross-section to changes in these parameters, $\underline{a}$ and R_o were changed in small steps about a "reasonable" value. This in effect also changes V_o, since this potential is always adjusted to give the correct binding energy. The calculations were made for the $f_{5/2}$ at 15.0 and 25.1 MeV and the results are summarized in Table VI. While the strength of the transitions varies, the shape of the angular distributions remains unchanged. In Table VI the strength was arbitrarily set to unity for R_o = 1.225 fm and $\underline{a}$ = 0.70 fm, the change in the strength was found to be independent of the energy of the incoming deuterons. Reducing either R_o or $\underline{a}$ has the effect of changing the well in which the neutron moves in such a way, that the wavefunction for the neutron is shifted to a smaller radius. This decreases the overlap with the distorted waves and therefore decreases the cross-section.

A change in λ changes the strength of the spin-orbit coupling. While the shape of the distributions is virtually unaffected, the change in cross-section is approximately proportional to $-\ell$ for $j = \ell + \frac{1}{2}$ transitions and proportional to $(\ell + 1)$ for $j = \ell - \frac{1}{2}$ transitions, as is to be expected. However, the effect is not as large as might be expected due to the fact that a change in λ is largely compensated by a change in V_o, since the computer program is written to adjust V_o to give the correct binding energy, B_N.

C. Triton Parameters: The parameters for the triton distorted waves are not well known, since no elastic scattering data are available. A "best guess" of their values was made and the two most doubtful, namely R_o', the radius of the imaginary potential, and W_o, the depth of the imaginary potential, were changed systematically to study their effect. This was done at 15 MeV for the $i_{13/2}$, $f_{5/2}$, and $f_{7/2}$ states. Since these parameters are expected to affect the shape of the distributions it was hoped that values could be found which would improve the fit to the experimental distribution for the $i_{13/2}$ at the forward angles. In fact, the shape was changed little for the $f_{5/2}$ and $f_{7/2}$, but was changed appreciably at the forward angles for the $i_{13/2}$ (see Figure 16). The change in the strength, or peak cross-section, found to be independent of the transition, was approximately 30 % for the range of W_o and R_o' investigated as shown in Table VII.

Two criteria were used in selecting the "best" parameters. These were the quality of fit to the shape of the $i_{13/2}$ at the forward angles and the fit to the absolute differential cross-section at all three energies. To obtain approximately the same spectroscopic factors at all three energies it was necessary to vary W_o from 17 MeV at E_d = 15 MeV to 22 MeV at E_d = 25.1 MeV. This was the only energy dependence found and it is not inconsistent with the energy dependence of optical model parameters found from the analysis of elastic scattering data of other particles.

All of the above calculations were made assuming the interaction to be of zero range. While the results are very good, to complete the investigation, the effects of other types of interactions were studied. Calculations were made in which the interaction was assumed to be of

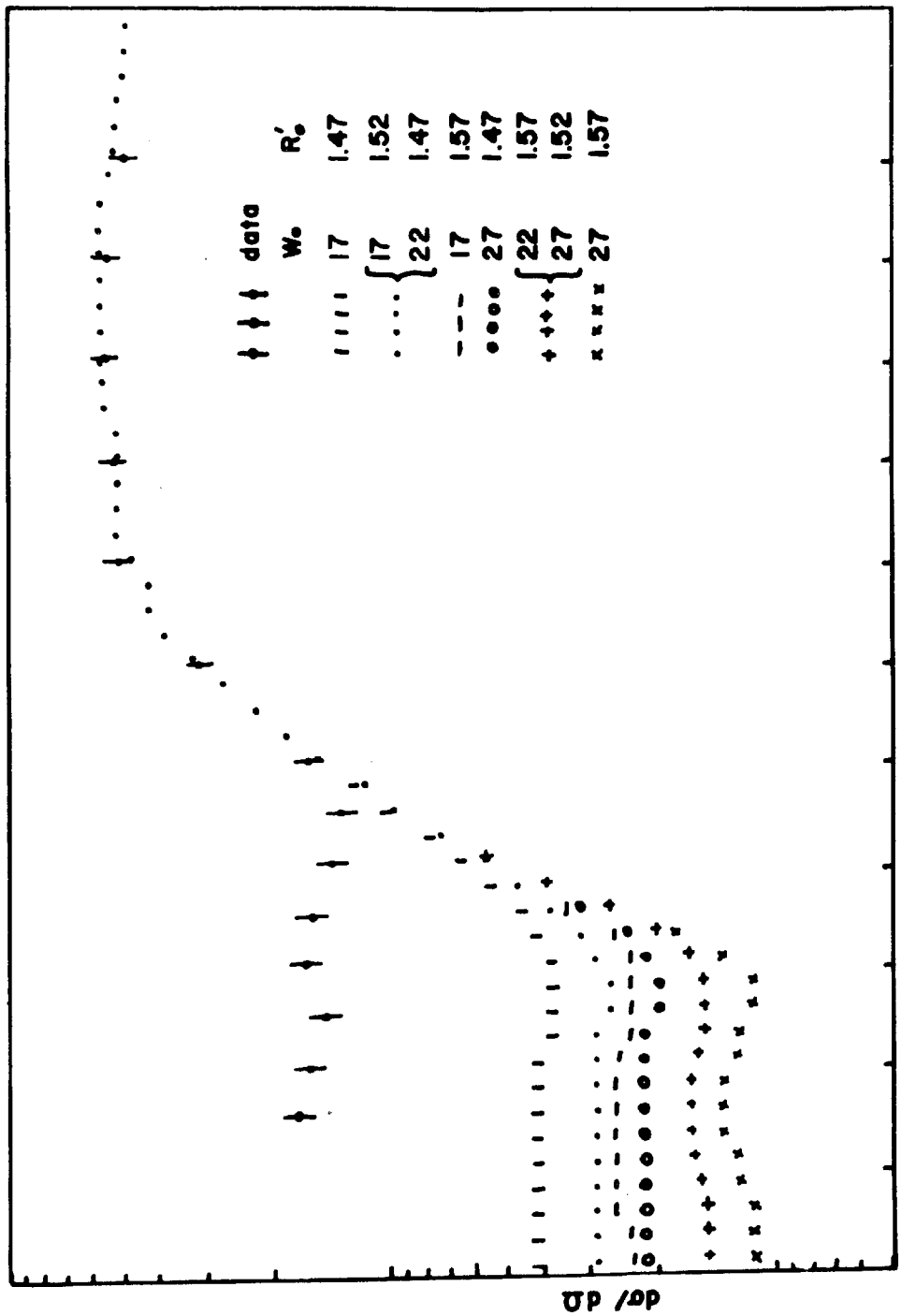

FIGURE 16 - Effect of Triton Parameters W_o and R'_o on Shape of Distribution of $i_{13/2}$

TABLE VI

Variation of Differential Cross-Section with Neutron Parameters R_o and $\underline{a}$

R_o \ $\underline{a}$	0.65	0.70	0.75
1.200	0.75	0.85	0.95
1.225	0.89	1	1.13
1.250	1.06	1.19	1.34

The value for R_o = 1.225 and $\underline{a}$ = 0.70 was arbitrarily called unity.

The results are for the $f_{5/2}$.

TABLE VII

Variation of Differential Cross-Section with Triton Parameters W_o and R_o

R_o' \ W_o	17	22	27
1.47	1.33	1.20	1.09
1.52	1.13	1	0.89
1.57	0.93	0.81	0.71

The value for R_o' = 1.52 and W_o = 22 was arbitrarily called unity.

The results are for E_d = 15 MeV.

finite range and in which the potentials (optical model as well as shell model potential) were assumed to be non-local [19, 20]. The corrections for both finite-range and non-local effects were made in the neutron wave function. The results of these calculations are shown in Table VIII. It was found that the finite range calculations increase the cross-section in many cases with respect to the zero range calculations. This result is expected in reactions in which the contribution to the cross-section due to the interior of the nucleus is small [21] as is the case in the ^{208}Pb(d,t) reaction.

In order to determine the sensitivity of the cross-sections to a change in the deuteron energy, calculations were made in which the energy was varied from 14.5 MeV to 15.5 MeV and also from 24.75 to 25.5 MeV. The results are shown in Figures 17 and 18 respectively.

TABLE VIII

Effect on Cross Section of Finite Range and Non-Local Corrections

Level	15 MeV			25 MeV		
	Zero Range	Finite Range	Finite R. Non-Local	Zero Range	Finite Range	Finite R. Non-Local
$p_{1/2}$	1.09	1.32	1.03	1.06	1.06	0.88
$p_{3/2}$	0.94	1.14	0.91	0.83	0.94	0.58
$f_{5/2}$	1.10	0.91	0.71	1.00	0.76	0.61
$f_{7/2}$	0.76	0.55	0.42	0.72	0.49	0.42
$i_{13/2}$	1.00	0.78	0.63	1.00	0.69	0.54

Shown are Spectroscopic Factors.

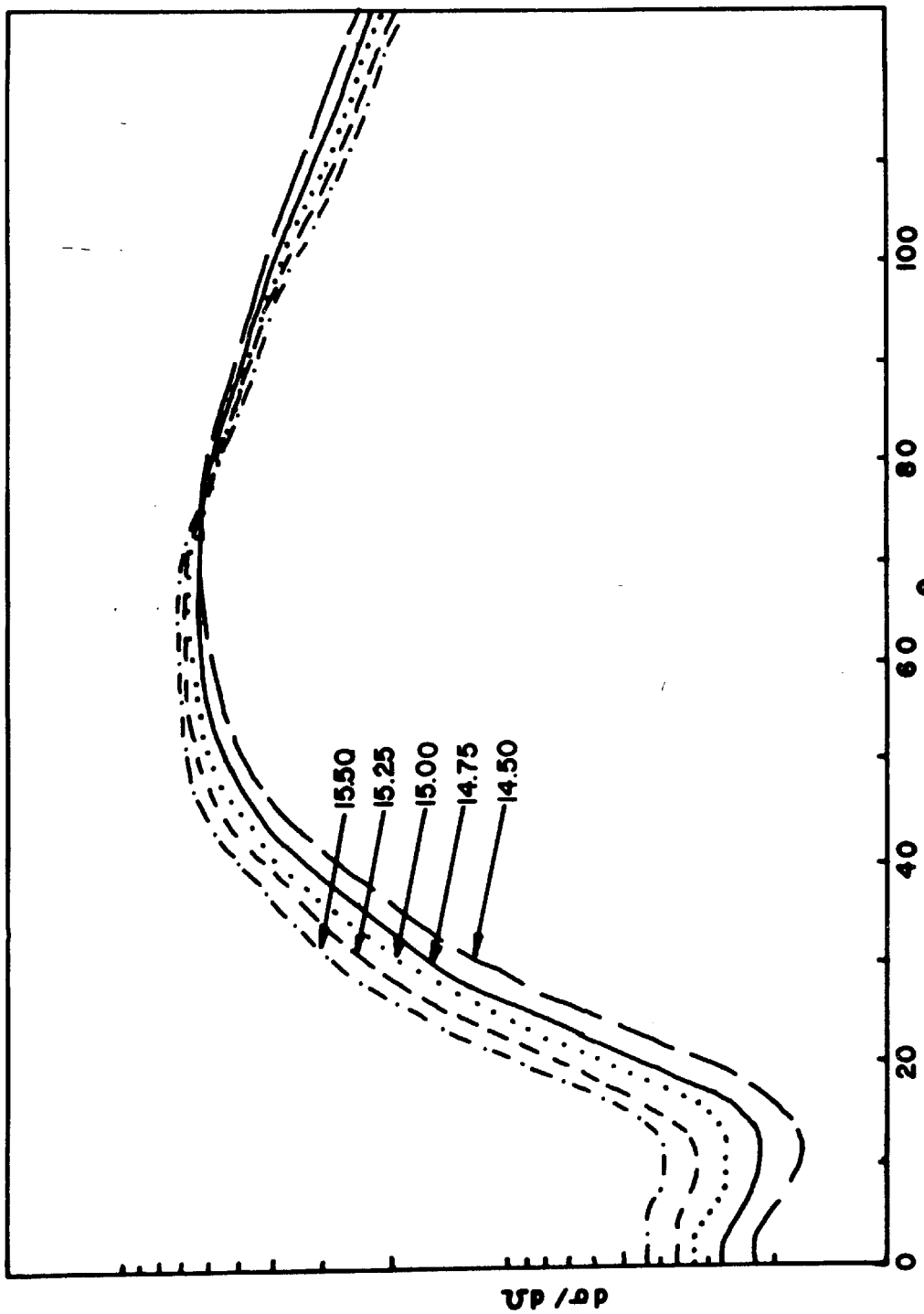

FIGURE 17 - Energy Dependence of $f_{5/2}$ at 15 MeV

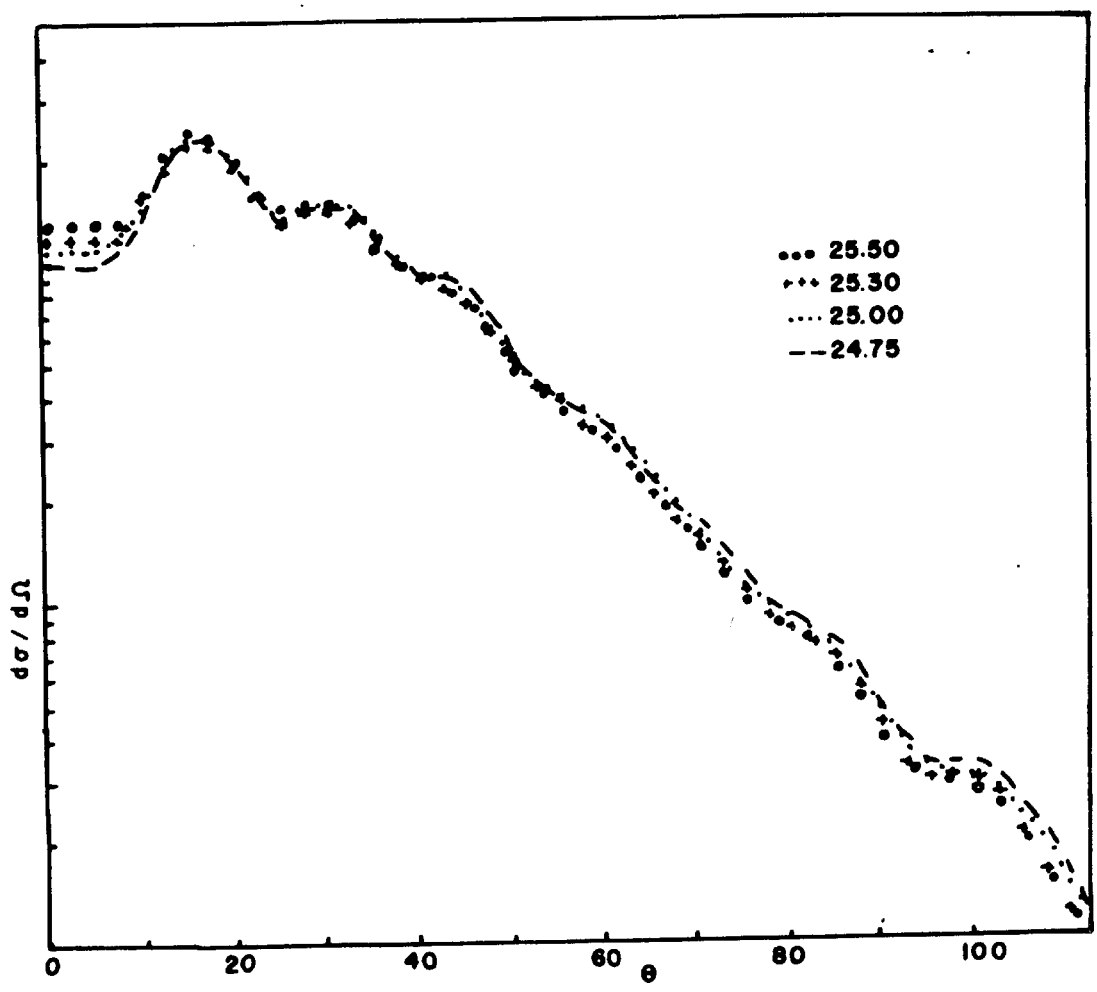

FIGURE 18 - Energy Dependence of $f_{5/2}$ at 25.1 MeV

CHAPTER V

SUMMARY AND CONCLUSION

The purpose of the work described in this dissertation was to determine experimentally the absolute differential cross-sections for the (d,t) reaction on ^{208}Pb for incident deuterons in the energy range from 15 to 25 MeV and to determine the set of parameters in the DWBA calculations that give the best fit to the measured differential cross-sections.

Differential cross-sections were measured for five single particle levels from 10^{o} to 100^{o} at three energies, namely 14.8 MeV, 20.1 MeV and 24.8 MeV. The level at an excitation energy of 3.43 MeV was identified as the $h_{9/2}$ single particle state. Differential cross-sections were also measured for elastically scattered deuterons from 25^{o} to 110^{o} at all three energies in order to determine possible energy dependence of the deuteron distorted wave parameters.

The DWBA calculations were performed for several values of the bound neutron parameters $\underline{a}$, R_o and λ, several values of the triton distorted wave parameters W_o and R_o' and different forms of the interaction.

It was found that the measured distributions could be matched well with calculated distributions in shape as well as absolute cross-section. The only major discrepancy found was for the $i_{13/2}$ at the lower energies and at forward angles.

Changing the triton distorted wave parameters W_o and R_o' affects the shape of the distributions at the forward angles, particularly for

the $i_{13/2}$. It was necessary to vary W_o with energy to obtain equally good fits to the absolute cross-sections at all three energies. The neutron parameters R_o and $\underline{a}$ were found to affect the absolute cross-section only. The amplitude of the interaction, D_o, has been calculated [15] and experimental evidence supports this value [23]. Calculations which included corrections for finite range and non-local effects did not improve the fit to the absolute cross-section.

Using the best set of parameters as determined in this investigation it was found that the shape of the calculated angular distributions agree well with the measured distributions. The absolute differential cross-sections differ by as much as 28 %. This relatively small disagreement in the absolute cross-sections is believed due to a spin-orbit effect; changing the strength of the spin-orbit coupling improved the agreement, but the effect was small, only a few percent.

The best set of parameters are essentially the same as those obtained for reactions in the lower mass regions and those in the mass region of lead but at lower energies [22, 23]. It is concluded therefore, that the DWBA analysis will be useful in extracting ℓ-values and spectroscopic factors in the heavy mass region for deuterons of energy 15 to 25 MeV.

REFERENCES

1. W. C. Parkinson, R. S. Tickle, P. Bruinsma, J. Bardwick and J. M..Lambert, Nucl. Instr. and Meth., 18, 19, 93-110 (1962).

2. H. W. Fulbright, J. A. Robbins, and A.K. Hamann, Univ. of Rochester, Rept. NYO-10261.

3. W. A. Aron, B.G. Hoffman, F.C. Williams, "Range-Energy Curves" Radiation Laboratory, Univ. of California, Berkeley, Report AECU-663, (Technical Information Service, 1951).

4. F. P. Brady, N. F. Peek and R.A. Warner, "Energy Levels from Electron Conversion in Pb^{207}", Univ. of California, Davis, Report CNL-UCD 23.

5. B. L. Cohen, Rev. Sci. Instr., 30, 415 (1959).

6. L. I. Schiff, Quantum Mechanics (Mc Graw-Hill, 1955) p. 99.

7. M. G. Mayer and J. D. Jensen, Elementary Theory of Nuclear Shell Structure (Wiley, 1955).

8. G. R. Satchler, "Some Topics in the Theory of Direct Nuclear Reactions", (Lecture Notes, Univ. of Colorado, 1965).

9. G. R. Satchler, Nuclear Physics, 55, 1 (1964).

10. M. A. Melkanoff, D. S. Saxon, J.S. Noderik, and D. G. Cantor, A Fortran Program for Elastic Scattering Analyses with the Nuclear Optical Model (University of California Press, 1961)

11. W. Tobocman, Theory of Direct Reactions (Oxford University Press, 1961).

12. N. Austern, in Fast Neutron Physics, Part II, ed. by J. B. Marion and L. J. Fowler (Interscience Publishers, 1963).

13. J. B. French, in Nuclear Spectroscopy, Part B, ed. by Fay Ajzenberg-Selove (Academic Press, 1960).

14. J. C. Gunn and J. Irving, Phil. Mag., 1353 (1951)

15. R. H. Bassel, "Normalization of and Finite Range Effects in (^{3}He,d) and (t,d) Reactions" (To be submitted for publication in Phys. Rev.)

16. L. D. Landau and E. M. Lifshitz, Quantum Mechanics (Addison-Wesley, 1958) p.434.

17. J. L. Yntema, Phys. Rev., 113, 261 (1959).

18. P. Mukherjee and B. L. Cohen, Phys. Rev., 127, 1284 (1962).

19. P. J. A. Buttle and L. J. B. Goldfarb, Proc. Phys. Soc., 83, 701 (1964).

20. Gy. Bencze and J. Zimanyi, Phys. Letts., 9, 246 (1964).

21. See reference 8, p. 6.19.

22. M. Dost and W. R. Hering, Phys. Letts., 19, 488 (1965).

23. W. R. Hering, M. Dost and U. Lynen, "Experimental Test of the Triton Form Factor by Coulomg-Pick-up on ^{208}Pb" (private communication in form of preprint).

24. W. C. Parkinson, private communication

25. E. Adelberger and C. A. Barnes, Bull. Am. Phys. Soc., 10, 1195, (1965).